JACS
JOURNAL OF THE AMERICAN CHEMICAL SOCIETY
pubs.acs.org/JACS
Article

Leveraging Quantum Chemistry and Machine Learning for the Design of Low-Valent Transition Metal Catalysts in Nitrogen to Ammonia Conversion

Chandrasekhar Nettem, Ankit Mondal, and Gopalan Rajaraman*

Cite This: J. Am. Chem. Soc. 2025, 147, 16948−16963
Read Online
ACCESS | Metrics & More | Article Recommendations | Supporting Information

ABSTRACT: The conversion of N_2 to NH_3 under ambient conditions is a major goal in sustainable chemistry. Homogeneous catalysts, particularly those employing cyclic(alkyl)-(amino)carbene (CAAC) ligands, have demonstrated promise in stabilizing low-valent Fe centers, yet industrial-level turnover numbers (TONs) and frequencies (TOFs) remain unmet. Here, we integrate quantum chemistry, molecular dynamics, and machine learning (ML) to uncover mechanistic features governing nitrogen reduction reaction (NRR) activity and guide catalyst design. Density functional theory (DFT) and ab initio molecular dynamics reveal that $[Fe(CAAC)_2]$ leverages redox noninnocent CAAC ligands to stabilize Fe(I) ($[Fe^{I}(CAAC)_2^{\bullet-}]$), with strong antiferromagnetic coupling ($J_{Fe\text{-}CAAC} = -1817\ cm^{-1}$). Flexibility of bulky Dipp groups found to hinder N_2 binding, rationalizing experimental observations. The exothermic formation of $[(CAAC(H))_2Fe]$ ($\Delta G = -4.5$ kJ/mol) with in situ generated H_2 exposure rationalizes the lower TON observed via catalyst deactivation. ML models trained on quantum descriptors such as M−C bond lengths, spin density, and frontier orbital energies identify the M−C distance as a key predictor of reactivity. A composite free energy metric (ΔG_{tot}) encompassing cis-trans isomerization (ΔG_1^0), N_2 binding (ΔG_2^0), and the first reduction step (ΔG_3^0) enables ranking of candidate catalysts. Moreover, Ti and V complexes show the lowest ΔG_{tot} (24−60 kJ/mol), while late transition and coinage metals exceed 120 kJ/mol, correlating with lower activity. By providing unprecedented insights into the interplay among ligand design, metal choice, and catalytic efficiency, this work lays a critical foundation for the rational design of homogeneous NRR catalysts, with implications for advancing sustainable ammonia production technologies.

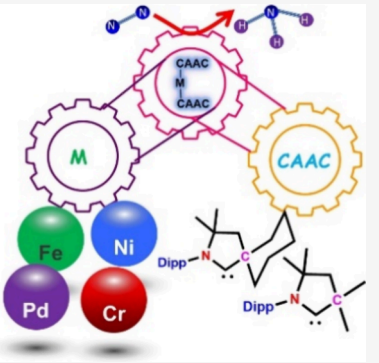

INTRODUCTION

Ammonia (NH_3) holds a pivotal position as a crucial chemical feedstock, contributing significantly to human food production and emerging as a promising candidate for high-density hydrogen carriers.[1−14] The Haber−Bosch process, employed for industrial ammonia production for over a century, necessitates stringent reaction conditions (350−550 °C and 150−350 atm pressure) to overcome slow reaction kinetics associated with activation of N_2.[15−17] This process of converting N_2 and NH_3 requires ∼485 kJ/mol of energy for the entire process.[18,19] Industrial ammonia production consumes nearly 1% of the global energy supply and emits over 300 million metric tons of CO_2 annually, primarily due to hydrogen production from fossil fuels, while the search for sustainable molecular catalysts with comparable efficiency remains challenging.[14,20,21]

The energy required for biological nitrogen fixation by bacterial nitrogenases is approximately 488 kJ/mol per N_2 molecule, primarily due to the ATP consumption needed to drive the reaction.[5,22−24] This is particularly significant due to the multimetallic catalytic site of the widely prevalent nitrogenase (FeMoco), enabling the efficient conversion of N_2 to NH_3 (with a turnover frequency of 2400 h^{-1} per reduced N_2) under ambient temperature and pressure conditions.[25,26] In the pursuit of developing artificial nitrogen fixation systems, chemists have predominantly directed their efforts toward creating synthetic functional analogues of nitrogenase using transition-metal complexes.[26] Despite the apparent impracticality of replacing the Haber−Bosch process with a more sustainable one based on molecular complexes in the near future, this approach stands as one of the most ambitious fundamental challenges.[27] Furthermore, it holds the promise of providing insights into the N_2 reduction mechanism and, ideally, identifying key factors (such as ligand design, role of metals and their spin-states, and reaction conditions) to enhance catalytic efficiency. Given that iron is the sole transition metal recognized as indispensable for enzymatic nitrogenase function and the primary transition metal catalyst employed in the Haber−Bosch ammonia synthesis, exploring

Received: January 3, 2025
Revised: April 20, 2025
Accepted: April 22, 2025
Published: May 3, 2025

https://doi.org/10.1021/jacs.5c00099
J. Am. Chem. Soc. 2025, 147, 16948−16963

the chemistry of N_2 reduction using well-defined iron model complexes is of considerable interest.[7−9,24,28]

In the molecular front, early work demonstrates the utilization of 4*d*/5d heavier analogs such as Mo and W that were found to reductively activate N_2 and produce NH_3, albeit with lower efficiency.[29] A search for earth-abundant metal for N_2 activation was achieved with the utilization of Fe in the year 2011 by Peters and co-workers (Scheme 1). Since then, a

Scheme 1. Various Molecular Catalysts Employed in Nitrogen Reduction Reaction (NRR) Reported in the Literature

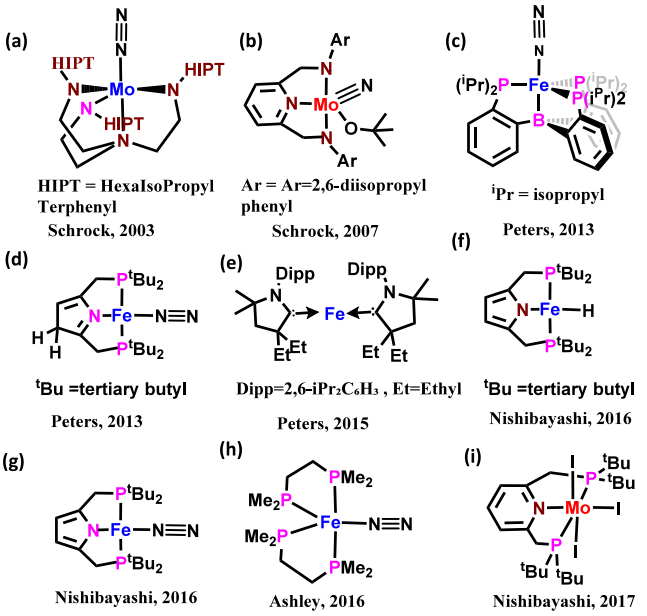

number of ligand and metal variants have been reported for the activation of N_2.[8−11] While the role of metal, coordination number, spin-state, and ligands in this process was not fully understood despite years of experimental efforts, the low-coordinate transition metal complexes were found to be very efficient in this process, particularly in the conversion of N_2 to NH_3.[30] A noteworthy experimental advancement comes from the Peters group, who employed a cyclic (alkyl)(amino)-carbene (CAAC), known for its π-accepting properties, to synthesize a structurally unconventional two-coordinate complex formally designated as $[(CAAC)_2Fe]$ (CAAC = cyclic (alkyl)(amino)carbene; Scheme 1).[31] The formation of this complex involved the reduction of its corresponding two-coordinate iron(I) cation, which binds to N_2 at low temperatures ($T \leq -80$ °C). Upon treatment with potassium graphite (KC_8) and $HBAr^F_4 \cdot 2Et_2O$, the complex catalytically reduces N_2 to ammonia, with a turnover number (TON) of 3.3 at −95 °C, and the reaction was found to occur only at lower temperatures, limiting its ability for any industrial-scale applications. Further, the mechanistic details associated with catalyzing the transformation of N_2 to NH_3, utilizing $[(CAAC)_2Fe]$, are presently not understood due to complexities associated with transition metal spin states and complex reactivity patterns. It is noteworthy that although various linear and low valent transition metal CAAC complexes, including Cr,[32] Mn,[33] Fe,[34] Co,[34−36] Ni,[37] Cu,[38] Zn,[39] Pd,[40] Pt,[40] Au,[41,42] and Ag,[41] have been synthesized, their reactivity toward nitrogen has not been established.

Computational tools have advanced significantly over the years, shifting from providing mechanistic insights and rationalizing experimental observations to incorporating cutting-edge techniques like machine learning (ML) alongside traditional first-principles methods such as density functional theory (DFT).[43−45] DFT has been extensively used to quantify structure−property relationships at the atomic scale, enabling accurate predictions of catalytic behaviors in homogeneous catalysis at a reasonable computational cost. Meanwhile, ML has proven effective in identifying intrinsic correlations between various properties, offering deeper insights into DFT-computed data sets.[46−49] The combination of DFT and ML holds great potential for accelerating the design and discovery of novel catalysts, providing a comprehensive understanding of their functionalities.[49] While this has been utilized in various homogeneous catalysis and materials discovery, there are no reports on the molecular catalyzed conversion of N_2 to NH_3, despite it being one of the grand challenges.

Considering all these aspects, in this work, we have explored the mechanistic pathways involved in the catalytic transformation of N_2 to NH_3 catalyzed by $[(CAAC)_2Fe]$. In our pursuit of a comprehensive understanding of nitrogen reduction reactions (NRR) catalyzed by linear and low-valent transition metals CAAC complexes, we expanded our investigation to other low-valent transition metal CAAC complexes with different CAAC ligands which have been synthesized and crystallized (Sc, Ti, V, Cr, Mn, Co, Ni, Cu, Zn, Ag, Au, Pd and Pt).[32−42] With these metals and the combination of different CAAC ligands reported in the literature, we have first established the key mechanistic steps in the conversion of N_2 to NH_3. In the proceeding step, we developed various descriptors for the N_2 to NH_3 conversion and ML models. This analysis provides significant design clues on rate-limiting steps and provides inputs on the nature of the metal-ion and CAAC ligand combination that are best suited to overcome the current limitations in terms of TONs.

COMPUTATIONAL METHODS

Static DFT Calculations. Density functional theory (DFT) computations were conducted using the dispersion-corrected unrestricted Becke3LYP (B3LYP-D3) hybrid functional.[50−54] A benchmark study was conducted to validate the ground-state characterization and ensure numerical accuracy in predicting spin-state splitting energies and the free energy differences between *cis*-*trans* isomers. This analysis assessed the reliability of the B3LYP functional by comparing its results for spin-state splitting energies, *cis*-*trans* free energy differences, and geometrical parameters to those obtained using various exchange-correlation functionals, including GGA functionals (BP86, PBE) and hybrid functionals (TPSSH, PBE0). Furthermore, previous studies have confirmed the accuracy of B3LYP in modeling transition metal systems involved in N_2 activation, reinforcing its suitability for this work. The LanL2DZ basis set with the Los Alamos effective core potential was employed for the transition metal (Sc−Zn) atom, while the 6-31G(d) basis set was used for the remaining atoms, including H, C, K, O, and N.[55,56] Molecular geometries were optimized without constraints using the Gaussian 09 suite of programs.[57] At the same level of theory, frequency calculations were performed to confirm the nature of the species and to compute enthalpic and entropic corrections, ensuring that all reported energies are free energies, unless stated otherwise. Minima and first-order saddle points were verified by zero and one imaginary frequency, respectively. Additionally, intrinsic reaction coordinate (IRC) calculations were conducted for selected geometries to validate the correct nature of the transition state. Single-point

https://doi.org/10.1021/jacs.5c00099
J. Am. Chem. Soc. 2025, 147, 16948−16963

Scheme 2. Mechanistic Cycle of Nitrogen Reduction to Ammonia by Low Valent Transition Metal CAAC Complexes $[(L)_2M]$[a]

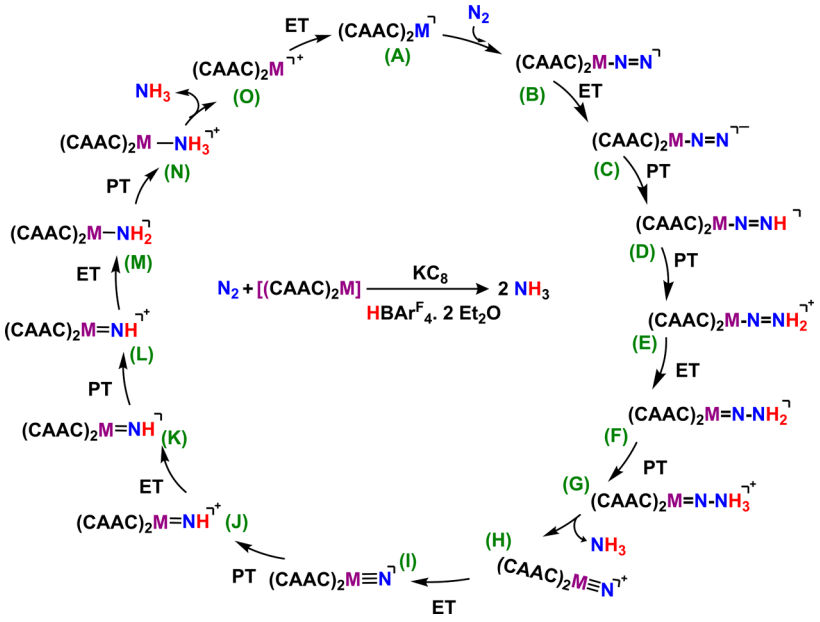

[a](M = transition metal, CAAC = cyclic (alkyl)(amino) carbene). Electron source: KC_8 and proton source: $HBArF_4{\cdot}2Et_2O$.

calculations were done on optimization geometries and transition structures with the TZVP basis set, along with the solvent. Solvent effects were incorporated by using a polarizable continuum model (PCM), with diethyl ether as the solvent, consistent with experimental conditions. All reported energies are Gibbs free energies, computed using electronic energy at the TZVP level with free energy corrections from LanL2DZ/6-31G(d) at 298.15 K. The experiments were conducted at 153−193 K, where entropic contributions, particularly in the initial steps of N_2 binding, are expected to diminish, influencing the overall free energy. However, for consistency, all calculations in the paper are reported at 298.15 K.

To evaluate and analyze the results obtained from B3LYP functionals, we conducted limited benchmarking studies incorporating additional functionals: PBE, BP86, PBE0, and TPSSH, all with dispersion corrections. Using these functionals, we estimated the spin-state splitting energy gap and the free energy associated with *cis*-trans isomerization. AIM (Atoms in Molecules), Localized orbital locator (LOL), Energy decomposition analysis (EDA), and NCI (Non-covalent Interactions) were performed on the optimized geometries employing G09, and Multiwfn 3.7.[58,59] EDA analysis was performed on various catalysts by considering three fragments: one metal and two CAAC ligands. Further, to understand the factors influencing the variation in nitrogen binding energies to different catalysts, we applied the activation strain model and energy decomposition analysis (EDA). The binding energy ΔG_{bind} of N_2 to different catalysts can be dissected into strain energy ΔE_{def}, representing the deformation of fragments ($\Delta E_{strain} = \Delta E_{sub}^{def} + \Delta E_{cat}^{def}$) during bond formation. This is coupled with the interaction energy ΔE_{int} between the deformed fragments, further divided into steric repulsion ΔE_{steric} and bonding orbital interactions ΔE_{orb}. Natural population analysis and HOMO−LUMO energies were determined from single-point calculations on the optimized geometries using the B3LYP functional and the TZVP basis set. The natural population analysis was performed by using the NBO program. The DFT-based Steric Parameters (DBSTEP) package was used to calculate the sterimol steric parameters and buried volume parameters, with all settings configured to default.[60] The buried volume ($\%V_b$) is measured by constructing a sphere (typically with a 3.5A radius) around the metal center atom and measuring how much of the sphere is occupied by the molecule. The magnetic exchange interaction between Metal (M) and ligand ($(CAAC)_2^{\cdot-}$) radical is described by the following spin Hamiltonian, $\hat{H} = -J$ S1.S2, where J is the isotropic exchange coupling constant.

Ab Initio Calculations. Additionally, we have also performed complete active space self-consistent field (CASSCF) calculations using the ORCA quantum chemistry package (version 5.0.0).[61−66] The scalar relativistic Hamiltonian was applied using the zeroth-order regular approximation (ZORA) method.[67] The RIJCOSX approximation with a def2/J auxiliary basis set was employed. Starting guess orbitals were obtained using the DFT method with ROKS/BP86 terminology, utilizing ZORA-def2-TZVP for metals, ZORA-def2-TZVP(-f) for N and O, and ZORA-def2-SVPfor C and H atoms.[68] For CASSCF/NEVPT2 calculations, the active space was defined as CAS(12,9), representing the five metal 3d orbitals and two p orbitals of each CAAC ligand, respectively. Single-point DLPNO-CCSD-(T)[65,69] calculations (cc-pVTZ; No Frozen Core, TIGHTPNO) were performed on the optimized geometries using ORCA,[70] employing a slightly simplified model to maintain computational feasibility while preserving key electronic features (see ESI for further details).

Ab Initio Molecular Dynamics (AIMD). Born−Oppenheimer molecular dynamics (BOMD) simulations were conducted using the CP2K code,[71,72] with the PBE/DZVP functional[73] for Fe and the PBE/TZVP functional for C, H, N, and O. This methodology has been demonstrated to produce reliable results in previous studies.[74] The velocity Verlet algorithm was employed with a time step of 1 fs, and a Nosé−Hoover thermostat was set to 300 K. Molecular structures and BOMD trajectories were visualized using the Visual Molecular Dynamics (VMD) package.[75] For the BOMD simulations of optimized systems, trajectories were propagated for 2000 fs at 300 K, and the valence electrons and atomic cores were described using Goedecker−Teter−Hutter (GTH) pseudopotentials.[76] The thermostat's time constant was set to 50 fs to ensure effective temperature control, with the simulation maintaining constant particle number (N), volume (V), and temperature (T) in an NVT ensemble. The ∠N1−C1−N2−C2 dihedral angles are reported directly as extracted from VMD without further transformation.

Machine Learning (ML) Tools. Machine learning studies were conducted using a variety of algorithms to analyze the data and predict outcomes. The models employed included linear models (linear regression, Lasso, Ridge, Elastic Net) and tree-based models (AdaBoost,[77] Random Forest,[78] gradient boosting, and Extreme Gradient Boosting[79−81]). All machine learning models were implemented using Python libraries such as scikit-learn, ensuring reproducibility and transparency in the analysis. For performance evaluation, metrics such as mean squared error (MSE), R-squared

https://doi.org/10.1021/jacs.5c00099
J. Am. Chem. Soc. 2025, 147, 16948−16963

(R^2), and mean absolute error (MAE) were utilized, with R^2 measuring how well the model explains the variation in the data, where values closer to 1 indicate a better fit. Each model was trained on the data set using a systematic approach to optimize hyperparameters and evaluate performance. Cross-validation was employed to assess the robustness of the models, ensuring that the predictions were not overfit to the training data. Given the small size of the training database, cross-validation was also conducted by using a leave-one-out (LOO) approach. The R^2 measures how well the model explains the variation in the data, with values closer to 1 indicating a better fit.[82] The LOO R^2 evaluates predictive performance by omitting one data point at a time, predicting its value from the remaining data, and then reassessing the model's fit. Unlike R^2, LOO R^2 does not necessarily improve with more parameters, making it a useful measure to avoid overfitting. Finally, we report the p-value from an F-test, which assesses the likelihood that the observed correlation is due to random chance. A lower p-value signifies a more statistically significant parameter. The F-test also adjusts for the number of parameters, thus avoiding a bias toward models with more parameters, similar to LOO R^2.

RESULTS AND DISCUSSION

Experimentally, [$(CAAC)_2Fe$] has been shown to convert N_2 and NH_3 with a TON of 3.3 at lower temperatures. While the TON and reactivity are lower compared to Mo catalysts, this is one of the best for the earth-abundant metal.[34] Further, X-ray and spectroscopic evidence, including IR, EPR, UV−vis, and Mossbauer spectra, indicate that the NRR proceeds via the binding of N_2 to the Fe center. Considering all these points and also the established NRR mechanism proposed in the literature,[83,84] we have adapted the mechanism shown in Scheme 2. Considering the fact that the ligands, metal ion, and its oxidation state play a key role in the NRR reaction, we aim to establish the electronic structure of the catalysts (A_{Fe}^{cis}, Scheme 1e) before we proceed to explore the mechanistic cycle.

This section of the manuscript is structured to systematically build toward the development of an ML-based catalyst design framework by exploring key electronic and mechanistic aspects of [$Fe(CAAC)_2$] and its analogs (i) we begin with a comprehensive discussion on the electronic structure of [$Fe(CAAC)_2$], addressing redox noninnocence, isomerism, and magnetic coupling between the metal center and CAAC ligands. Additionally, we examine the binding pocket evolution over time and quantify noncovalent interaction strengths. (ii) Next, we provide a brief electronic structure description of the N_2-bound species [$Fe(N_2)(CAAC)_2$], analyzing key factors influencing activation, including agostic/anagostic interactions within the binding cavity. (iii) We then present a detailed mechanistic study of the stepwise reduction, protonation events, and NH_3 release in the catalytic cycle of [$Fe(CAAC)_2$]. (iv) To rationalize the experimentally observed low TONs, we investigate potential degradation pathways, side reactions, and competing processes that limit catalytic efficiency. (v) To broaden the scope, we extend our analysis to [$M(CAAC)_2$] complexes (M = Sc−Cu, Pd, Pt, Ag, Au, CAAC = ^{Et}CAAC, ^{Me}CAAC, and ^{Cy}CAAC), systematically exploring the N_2 activation potential of 13 transition metals. (vi) Finally, insights from the computational study are leveraged to build an ML model, establishing a predictive framework for screening catalysts with improved efficiency, thereby guiding future experimental efforts in N_2 activation.

Electronic Structure and Dynamics of the [$(CAAC)_2Fe$] Catalyst. The [$(CAAC)_2Fe$] (A_{Fe}^{cis}), expected to have Fe atoms in zerovalent state, if the CAAC ligand is innocent, and this would lead to a formal $3d^64s^2$ configuration with three different spin states, S = 0, S = 1, and S = 2 states. Our calculations (see computational details) reveal S = 1 as the ground state, with S = 2 and S = 0 found to lie at 39.0 and 205.7 kJ/mol, higher, respectively. The S = 1 ground state predicted by the B3LYP functionalis consistent with the experimentally estimated magnetic moment of 3.0 μB, along with other spectroscopic data.[85] The computed geometrical parameters for the S = 1 state are also consistent with the X-ray geometry (see Tables S1, S2, Figures S1 and S2).[85] The Fe−C1 and Fe−C2 bond lengths of the ground state of optimized geometry are 1.962 and 1.961 Å, respectively (see Figure 1).

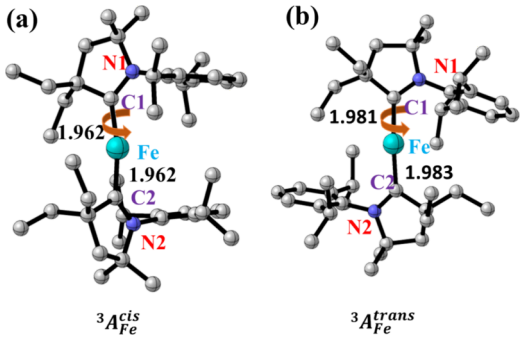

Figure 1. DFT computed geometries of (a) $^3A_{Fe}^{cis}$ and (b) $^3A_{Fe}^{trans}$complexes. The curved arrow indicates the axis of the dihedral angle rotation (N1−C1−C2−N2).

The C1−Fe−C2 angle in A_{Fe}^{cis} is modestly bent [169.34°] differs from the two-coordinate iron complex [{$((Me_3Si)_3C)_2Fe$}{K(2,2,2-crypt)}] which is almost perfectly linear (179.2°) but consistent with the X-ray geometry (169.5°).[85] As evidenced by the computed dihedral angles ∠N1−C1−C2−N2 of −72.12° (in A_{Fe}^{cis}), the nonplanar five-membered rings of the CAAC ligands are placed in a coplanar form and a *cis*-arrangement of the nitrogen atoms. A closer look at the electronic structure computed reveals a spin density of 3.10 on iron (Fe), and the CAAC ligand has individual contributions of −0.42 for C1 and C2, exhibiting a collective spin density of −0.84 in the S = 1 spin state, which arises due to antiferromagnetic coupling between the Fe center and the CAAC ligand with estimated J value of −1817.5 and −922.1 cm^{-1} for *cis* and *trans* isomer of catalyst.[34] This underscores the ligand's redox noninnocent behavior and suggests [$Fe^{I}(CAAC)_2^{\cdot-}$] as the electronic structure of the catalyst. Furthermore, the ground state optimized structure reveals several noncovalent anagostic weak interactions between hydrogens of methyl groups of CAAC with an iron atom with differing strengths confirmed by structural parameters (Fe···H bond lengths 2.4−3.2 Å; Fe···H−C bond angles 134−145°), ELF, LOL values (see Table S3 and Figure S3). The NBO analysis reveals that Fe−C1/C2 bonds are found to be single bonds (WBI of 0.73) and are significantly ionic (35% from Fe(d_{xy}) and 64.0% of C(p_y); see Figure S4 and Tables S4−S6). The electronic configuration for A_{Fe}^{cis} is found to be $(d_z^2)^{\uparrow\downarrow}$ $(d_{xz} + L\pi_y)^{\uparrow\downarrow}(d_{yz} + L\pi_z)^{\uparrow}(d_{x^2-y^2})^{\uparrow}(d_{xy,})^{\uparrow}(L\pi_y^* + d_{yz})^{\downarrow}(L\pi_y^* + d_{xz})^0$ (L = CAAC; see Figure S5). The d_z^2 orbital stabilization compared to $d_{xy,}$ orbital might be due to strong M···H−C anagostic[86] interactions present in the XY plane and s-d mixing[87] (see Table S3 and Figure S5).

https://doi.org/10.1021/jacs.5c00099
J. Am. Chem. Soc. 2025, 147, 16948−16963

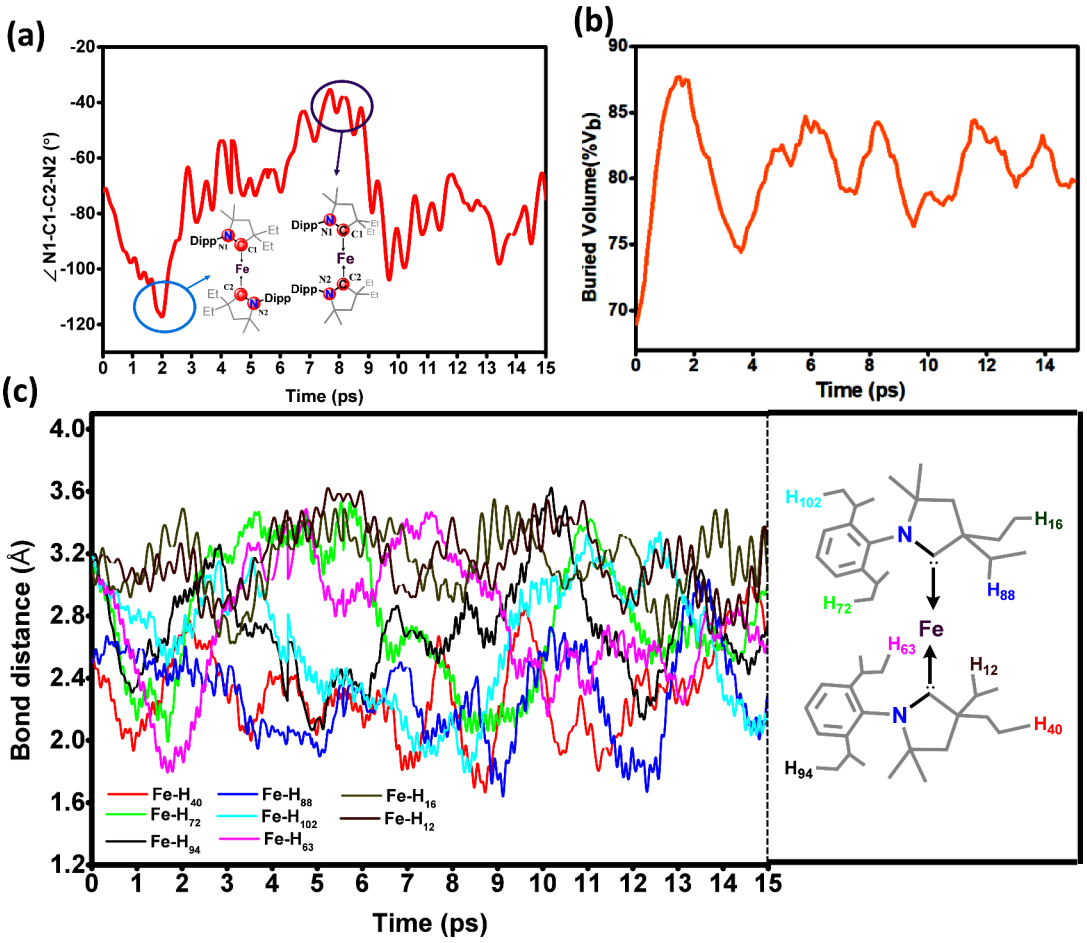

Figure 2. Selected structural parameters from the AIMD simulations of complex [$(CAAC)_2$Fe] (a), ∠N1−C1−C2−N2 dihedral angle (in °) during simulation (b), buried volume (%V_b) evolution during simulation, and (c) different C−H···Fe interactions during simulation (in Å).

We have also explored the other conformer A_{Fe}^{trans}, which is found to be 7 kJ/mol (ΔG_1^0; 7 kJ/mol) higher compared to A_{Fe}^{cis} with the ∠N1−C1−C2-N2 of −133.77° and ∠N1−Fe−C2 of 168.7°. The higher energy of the A_{Fe}^{trans} isomer is attributed to the strain energy in each CAAC ligand, calculated as 29.3 and 27.3 kJ/mol in the trans configuration, compared to 22.0 kJ/mol for both ligands in the *cis* isomer. A relaxed scan of ∠N1−C1−C2−N2 reveals energy alteration of rotation is ∼10 kJ/mol, suggesting a possible free rotation of the molecule at room temperature (see Figure S6).

Given the small energy difference and the observation that N_2 coordination occurs only in a certain temperature range, it is crucial to investigate the dynamics of CAAC movement over time. To this end, we have employed ab initio molecular dynamics simulations (AIMD) and performed NVT simulations for 15 ps (see Figure 2). AIMD simulations reveal that Fe···H_{CAAC} distances fluctuate between 1.6 and 3.6 Å, while Fe1−C1 and Fe1−C2 bond lengths vary between 1.77 and 1.99 Å. The ∠C1−Fe1−C2 angle decreases rapidly to 142° within the first 2 ps and then fluctuates between 160° and 180°, while the ∠N1−C1−N2−C2 dihedral angle decreases to −117° at 2 ps and later stabilizes between −100° and −60° after 10 ps (Figure 2a). Buried volume analysis of AIMD snapshots reveals that the tumbling motion of CAAC ligands causes the buried volume to oscillate between 75 and 85% (Figure 2b). As the Fe···H distances fluctuate, the nature of noncovalent interactions evolves, with anagostic interactions intermittently switching on and off, potentially rendering the metal site accessible for further reactions[88] (see Figure 2c); we decided to investigate these dynamics further to understand their role in this behavior and the absence of N_2 binding at room temperature for catalyst A_{Fe}^{cis}. The anagostic Fe···H interactions found at the equilibrium geometry were found to turn into agostic interactions at various snapshots during the MD simulation (see Figure S7).

Activation of Nitrogen by [Fe($CAAC_2$)]. The activation of the N_2 molecule is a critical step in the nitrogen reduction reaction (NRR). Due to the inert nature of N_2, a strong donation from the metal to the π^* orbital of N_2 is essential to weaken the N≡N bond. This process is complemented by the electron donation from N_2 to the metal via back-bonding, facilitating strong Fe−N_2 binding. The activation of nitrogen proceeds through the prereactive complex, in which, N_2 anchored to the catalyst via noncovalent interactions (H_{CAAC}···N_2) (reactant complex; $\mathbf{RC}^{AB}$) (see Figure S8 and Tables S7−S17), leading to the formation of a reactant complex which is found to be endergonic for both A_{Fe}^{cis} and A_{Fe}^{trans} by 23.5 and 31.4 kJ/mol, respectively (see Figure 3). In the next step, nitrogen binding to the metal proceeds via $^3\mathbf{TS}^{AB}$-*cis* ($^3\mathbf{TS}^{AB}$-*trans*), which has a kinetic barrier of 99.2 kJ/mol (70.3 kJ/mol) for A_{Fe}^{cis} (A_{Fe}^{trans}) isomer. A relatively larger barrier for the N_2 binding is associated with the need to elongate the Fe−C bonds to accommodate N_2, and this elongation is larger for *cis* than for the *trans* isomer, as reflected

https://doi.org/10.1021/jacs.5c00099
J. Am. Chem. Soc. 2025, 147, 16948−16963

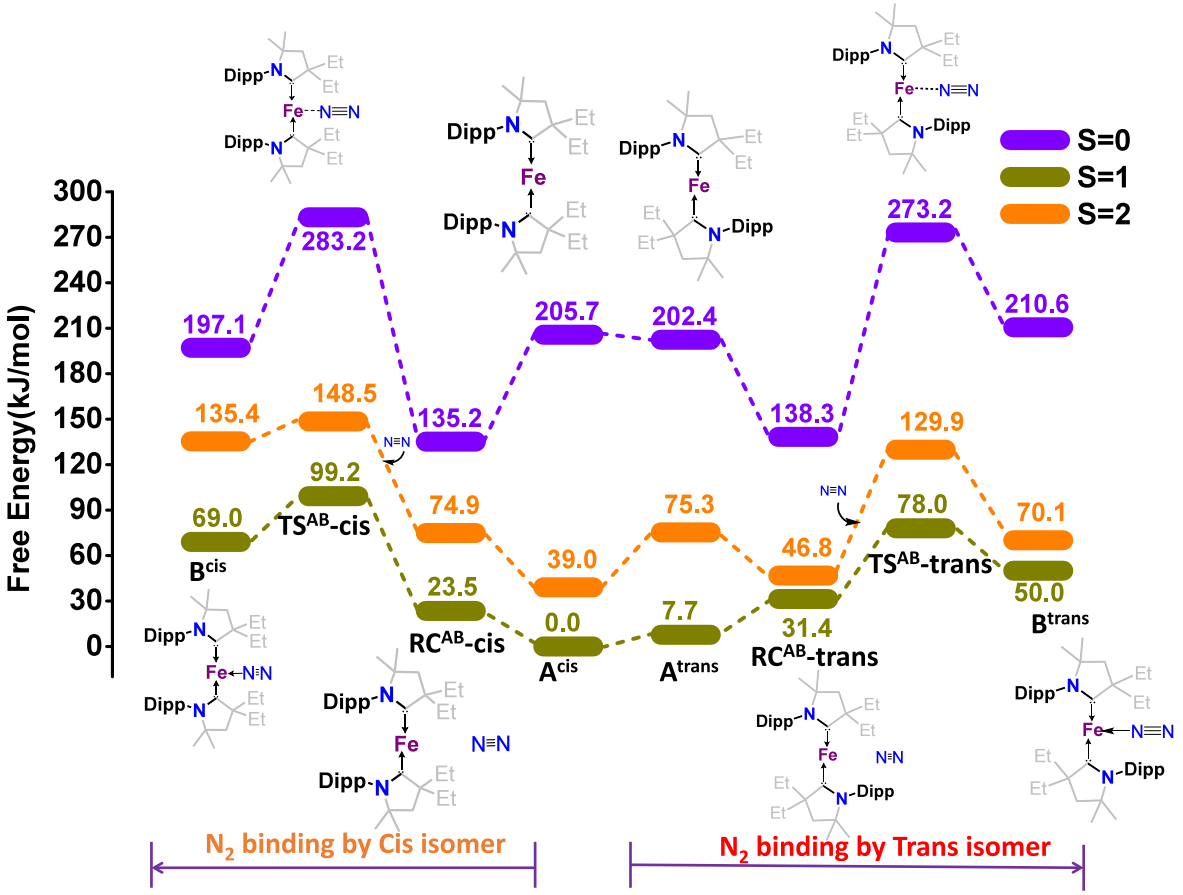

Figure 3. DFT computed energy profile for nitrogen binding to the *cis* and *trans* isomers of the catalyst [$(CAAC)_2Fe$] (all energies are given in kJ/mol).

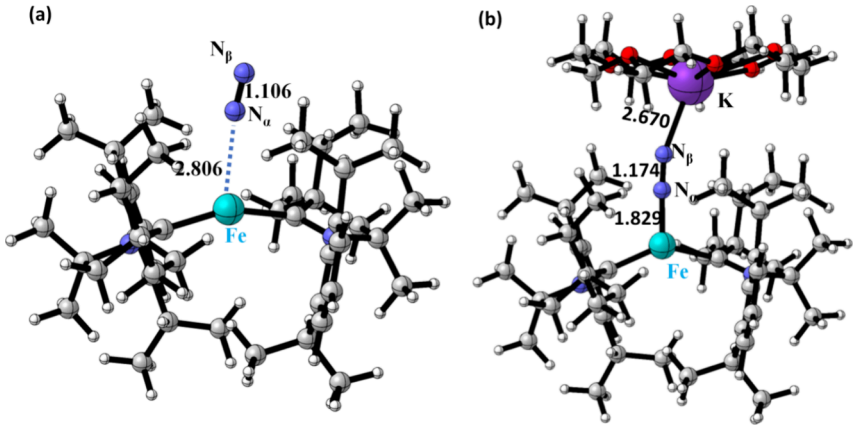

Figure 4. DFT computed geometries of (a) $^3TS^{AB}$-trans and (b) $^2C_{Fe}^{trans}$-K^+ [$(CAAC)_2Fe(N_2)$][K(18-crown-6)].

in the activation strain energy analysis[89,90] (see Figures S9 and S10). Dinitrogen coordination to the A_{Fe}^{cis} and A_{Fe}^{trans} yields B_{Fe}^{cis} and B_{Fe}^{trans}, respectively. This process is computed to be endergonic, with Gibbs free energy changes of 69.0 and 42.3 kJ/mol for A_{Fe}^{cis} and A_{Fe}^{trans}, respectively (see Figure 3) at 298 K. The reaction enthalpy is computed to be exothermic at −4.9 kJ/mol, but significant entropic contributions make it endergonic. At 153 K, where experiments were conducted, the free energy change decreases to ∼20 kJ/mol, indicating that lower temperatures mitigate unfavorable entropy effects, making N_2 binding more feasible, as reported elsewhere.[91] Given the inherent approximations in entropic estimates, N_2 binding is expected to occur, albeit weakly. Due to the weak N_2 binding, the turnover number (TON) of [$Fe(CAAC)_2$] is limited to ∼3.3, highlighting its low catalytic efficiency. The Fe−N1 bond distance in (B_{Fe}^{trans}) is 1.916 Å (see Figures S11, S12, Tables S18 and S19). The Fe−N−N linkage slightly deviates from the linear geometry (164.2° in B_{Fe}^{cis}, and 169.9° in B_{Fe}^{trans}) with end-on binding of N_2. With the *cis* isomer having a ∼30 kJ/mol higher energy barrier and an additional ∼20 kJ/mol penalty for N_2 binding, and given the facile *cis*-to-trans conversion, the reaction is expected to proceed via the *trans* isomer, and this is also consistent with the X-ray structure of N_2 bound to catalyst A_{Fe}.[85]

https://doi.org/10.1021/jacs.5c00099
J. Am. Chem. Soc. 2025, 147, 16948−16963

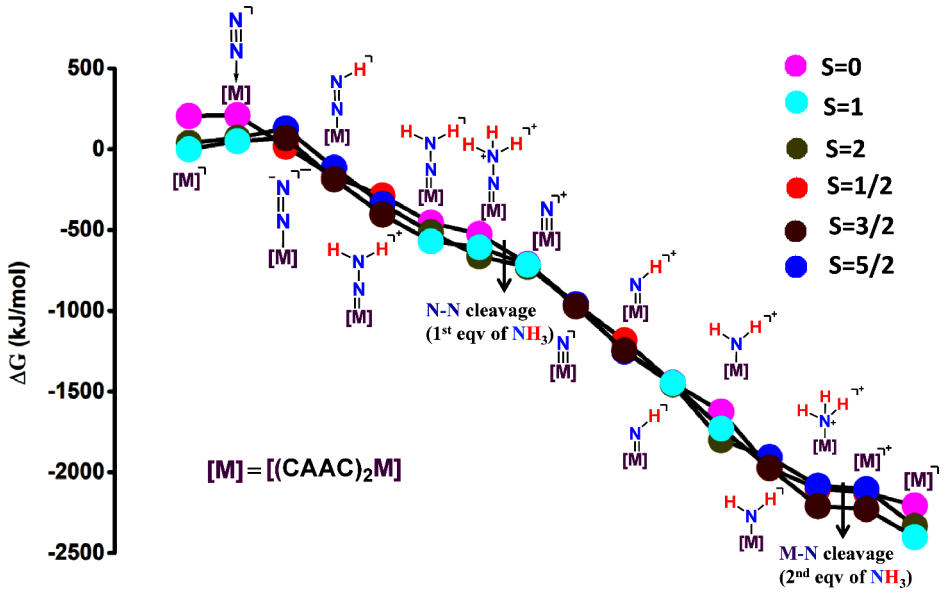

Figure 5. Free energy profile for the reduction of dinitrogen to ammonia catalyzed by $[(CAAC)_2Fe]$ upon treatment with KC_8 and $HBArF_4{\cdot}2Et_2O$ at 298.15 K and 1 atm pressure.

A limited benchmark study employing a range of exchange-correlation functionals within DFT (B3LYP, BP86, PBE, TPSSh, and PBE0), role of solvent in the optimized geometries, and ab initio calculations (CASSCF/NEVPT2 and DLPNO−CCSD(T)) was conducted to validate numerical accuracy in predicting the free energy differences between *cis*-trans isomers (ΔG_1^0) and nitrogen binding energies (ΔG_2^0) (see Tables S20−S24). Among the tested functionals, B3LYP provided a reliable numerical estimate for spin-state splitting/thermodynamics compared to those of other exchange-correlation functionals, showing good agreement with ab initio calculations. The inclusion of solvent does not affect the overall trend, though it causes slight variations in individual species' energies Furthermore, CASSCF/NEVPT2 and DLPNO−CCSD(T) calculations also predict $\boldsymbol{A}_{Fe}^{cis}$ to be the ground state consistent with DFT, although the estimated gap was slightly higher as DFT geometries were employed (10−15 kJ/mol; see Figure S13 and Tables S20−S24).[69,92]

A relaxed scan along the Fe···N≡N coordinate reveals that N_2 can approach only from one cavity (top and bottom) as other directions are blocked by strong C−H···π interactions and bulky groups (see Figures 4a and S14). Even in the cavity where N_2 is approaching, there are weak C−H···Fe agostic interactions, and as the N_2 moves closer to the cavity, these interactions break away, adding to the energy penalty. Furthermore, as N_2 approaches, several C−H···N≡N interactions appear and serve as one of the driving forces for N_2 coordination to the metal ion. Further, even at a longer Fe···N≡N distance of 2.7 Å, the N−N bond is elongated due to the donation of electrons to the π^* orbital of N_2 by the noncovalent interactions coupled with long-range electron transfer from the Fe atom (see Tables S25 and S26). Particularly, the d_{xz} + Lπ_y orbital was found to lie in the direction of the approach of N_2, leading to a stronger donation from this orbital upon binding, and this is exemplified by the EDA-NOCV analysis (∼80 kJ/mol; see Figure S15). As this orbital has a strong donation from the CAAC π(C−N) orbital, this illustrates the importance of a strong π donor ligand coupled with a low-valent metal for activating small inert molecules such as N_2. This also supports the experimental report where the N-heterocyclic carbene (NHC) ligand fails to activate the N_2.[31] At $\boldsymbol{B}_{Fe}^{trans}$ when the N_2 binds to Fe, a substantial negative charge transfer of −0.22 e (total proximal and distal) to π^* orbital of the N_2 is detected with more than 70% of this transfer remains in distal nitrogen atom, N_β and this indicates a higher susceptibility to protonation/reduction of this N atom compared to proximal nitrogen atom N_α (see Table S26). Buried volume analysis of AIMD snapshots reveals that the tumbling motion of CAAC ligands causes the buried volume to oscillate between 75% and 85% (Figure 2b), significantly shielding the metal center and hindering nitrogen binding. This dynamic behavior intensifies with thermal energy, aligning with experimental findings where nitrogen binds and converts to NH_3 below 193 K but remains unbound above this temperature; introducing linkers to reduce ligand tumbling could potentially enable nitrogen binding at elevated temperatures.

Mechanism of N_2 to NH_3 Conversion. In the next stage, reduction of $\boldsymbol{B}_{Fe}^{trans}$ by KC_8 in the presence of 18-crown-6 yielded the $[(CAAC)Fe(N_2)]$ $[K^+(18\text{-crown-6})]$ ($\boldsymbol{C}_{Fe}^{trans}$-$\boldsymbol{K}^+$) via an endergonic reaction (ΔG_3^0; 17.6 kJ/mol) for the S = 1/2 ground state with other spin-state found to lie higher in energy (52.2 and 110.8 kJ/mol for S = 3/2 and S = 5/2 states, respectively, see Figures S15−S18). Additional computational experiments performed suggest an electrostatic interaction to the tune of 78.5 kJ/mol between the potassium cation and the distal nitrogen atom (Figures 4b and S16−S19). At this stage, ∼0.90 e from KC_8 is found to be transferred to the catalyst. This suggests that following the electronic structure of $\boldsymbol{C}_{Fe}^{trans}$-$\boldsymbol{K}^+$ as $[(CAAC^{\downarrow})^{\cdot-}{}_2Fe^{I\uparrow\uparrow\uparrow}(N2)^{\cdot-\downarrow}]$, leading to the formation of S = 1/2 ground state, consistent with the experimental EPR and magnetic data.[31] Further, the computed structural parameters are consistent with the reported X-ray structure (see Tables S27−S30).[31] Notably, in the $\boldsymbol{B}_{Fe}^{trans}$ species, the $\pi^*(N_2)$ orbital lies lower in energy compared to the π(C−N)* and Fe(d_{xz}) orbitals, enabling stronger electron donation to N_2 and facilitating its protonation in the next step (see Figure S19). If the electrons had been directed toward CAAC or Fe

https://doi.org/10.1021/jacs.5c00099
J. Am. Chem. Soc. 2025, 147, 16948−16963

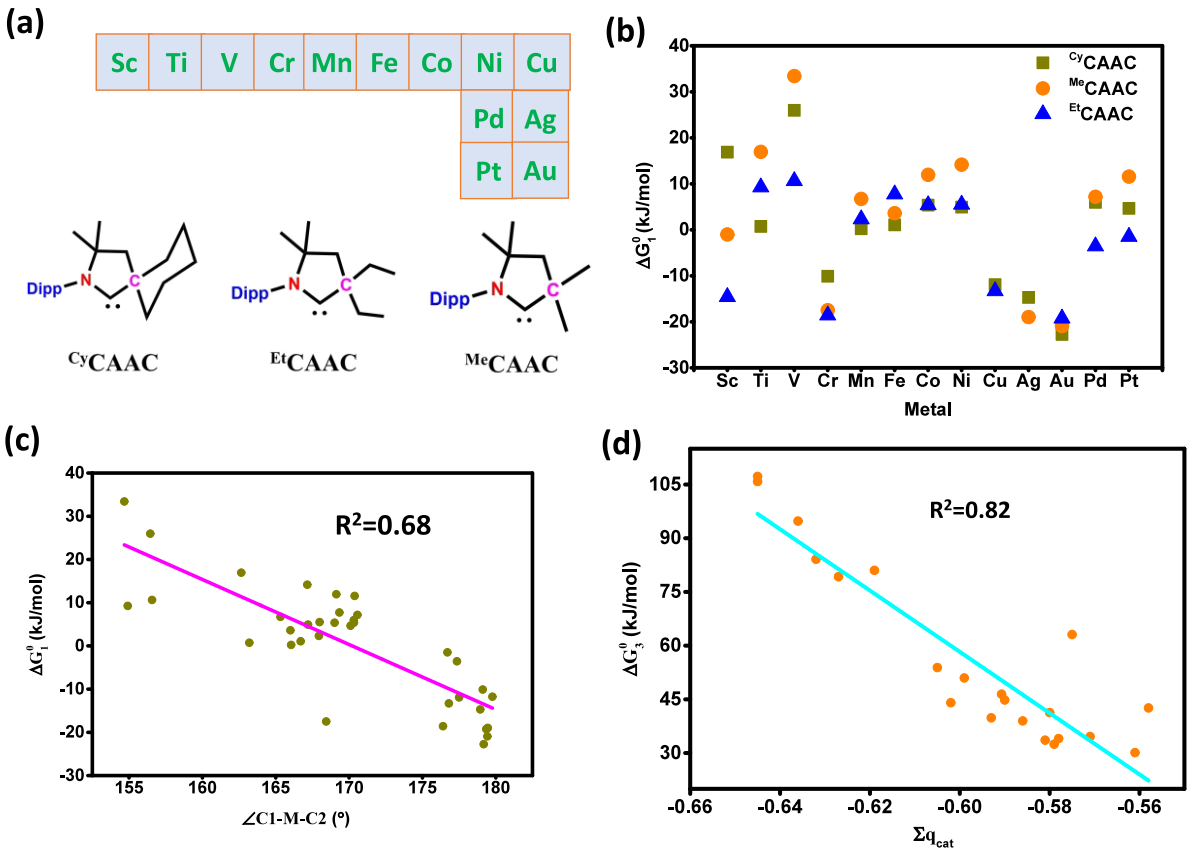

Figure 6. (a) Different metal and CAAC ligands used for ML model, (b) variation of cis-trans free energies for different metals, (c) correlation of the ∠C1−M−C2 angle with the ΔG_1^0, (d) correlation of sum of natural charges ($\sum q_{cat}$) with the ΔG_3^0 ($\sum q_{cat} = q_M + q_{C1} + q_{C2} + q_{N1} + q_{N2}$, where q_M, q_{C1}, q_{C2}, q_{N1}, q_{N2} is the natural charge of the M, C1, C2, N1, and N2 atoms, respectively).

instead, protonation—essential for NH_3 formation—would likely have been hindered. Thus, the noninnocence of the CAAC ligand and the precise energy ordering of the orbitals are critical for the reaction's success.[93]

In the subsequent catalytic cycle, protonation of $\mathbf{C}_{Fe}^{trans}$-$\mathbf{K}^+$ by $HBAr^F_4$ is assumed, and this is estimated to be a significantly exergonic process (210.3 kJ/mol), leading to the formation of $[(CAAC)_2FeNNH]$ ($\mathbf{D}_{Fe}$), with S = 3/2 ground state (see Figures S15 and S19). This is accompanied by a significant decrease in bond order for Fe−N_α, Fe−C1, and Fe−C2 bonds (see Figures S16 and S17). The spin density analysis reveals that N−H bond formation takes place by concomitant reduction of unpaired electrons from the CAAC and N_β moieties (see Tables S31−S38 and Figure S19). This electron shuffling within species $\mathbf{D}_{Fe}$ leads to enhanced charge polarization, with a positive charge on the Fe (0.422) and a significant negative charge of −0.763 on the dinitrogen.[36] Such a charge polarization generates a strong dipole and local electric field that aids the reaction further down the mechanistic cycle.[94] The terminal nitrogen retains most of this negative charge (−0.422), suggesting the possibility for facile second protonation. Keeping this in mind, we have computed a second proton transfer leading to the exogenic formation (218.9 kJ/mol) of the iso-diazene complex, $[(CAAC)_2FeN{=}NH_2]^+$ ($\mathbf{E}_{Fe}$) with an S = 3/2 ground state (see Figures S20−S31).

A substantial charge accumulation on the Fe atom in $\mathbf{E}_{Fe}$ necessitates an ET step to proceed forward, leading to the exogenic formation (166.1 kJ/mol) of $[(CAAC)_2FeN{=}NH_2]$ ($\mathbf{F}_{Fe}$) with an S = 1 ground state. In species $\mathbf{F}_{Fe}$, the nitrogen atoms possess significant negative charges and subsequently undergo protonation to form $[(CAAC)_2FeN{=}NH_3]^+$ ($\mathbf{G}_{Fe}$) species exogenically (92.7 kJ/mol at S = 2 ground state). At this species, the N−N bond length is significantly elongated (1.426 Å), with $\mathbf{N}_\beta$ possessing a significant positive charge that aids N−N bond cleavage in the next step, leading to the formation of $[(CAAC)Fe(N)]^+$ ($\mathbf{H}_{Fe}$−65.3 kJ/mol for S = 2 states). This is followed by the next six steps ($\mathbf{I}_{Fe}$ to $\mathbf{N}_{Fe}$), wherein Fe≡N undergoes consecutive exergonic PT and ET, leading to the release of the next molecule of NH_3 with various spin-state switching found to occur across the path (see Figure 5). To this end, it is clear from the energetics developed that in the entire catalytic cycle developed, the binding of dinitrogen to the catalyst (A_{Fe}^{cis}) is a key step, with a significant energy penalty for the subsequent ET step to generate species $\mathbf{C}_{Fe}^{trans}$-$\mathbf{K}^+$.[36] The exergonic nature of the catalytic cycle is evident from its highly negative free energy (−2408.7 kJ/mol; Figure 5). However, the overall process requires a free energy input of +2368.5 kJ/mol per N_2 (see Figure S32 and related text), making the catalyst less efficient than Haber-Bosch and nitrogenase in comparison. The proton and electron source here (KC_8 and $HBArF_4{\cdot}2Et_2O$) compensate for the energy demand, making this reaction feasible at the given reaction conditions.

Deciphering the Origin of Low TON for NRR. In general, NRR reactions are limited by low TON, with the best homogeneous catalysts achieving TONs below 100,[10,22] making them unsuitable for industrial applications or as a

https://doi.org/10.1021/jacs.5c00099
J. Am. Chem. Soc. 2025, 147, 16948−16963

replacement for the Haber-Bosch process. The catalyst that we have studied here has abysmally small TON (3.3 ± 1.1), and our mechanistic study hints at favorable thermodynamics with KC_8 and $HBAr^F_4$ effectively demonstrating 6e reduction and protonation all the way to the regeneration of the catalyst. This hints at other possible side reactions that act as catalytic poisoning to yield poorer performance in terms of efficiency. It has been well demonstrated in the literature that the reaction of KC_8 and $HBAr^F_4$, even in the absence of the catalyst, generates H_2, the production of which has been viewed as a significant hurdle in NH_3 production.[10,22,95] The reaction of H_2 with the catalyst A^{cis}_{Fe} is expected to be facile, and hydrogen is expected to add to the carbene carbon atom as demonstrated earlier in the $[Mn(CAAC)_2]$ reaction.[33,39] We hypothesize a similar reaction with catalyst A^{cis}_{Fe} with H_2, leading to the formation of $[(CAAC(H))_2Fe]$ ($\mathbf{Q_{Fe}}$), which does not have the ability to bind nitrogen and perform NRR (Figures S33−S35). The formation of this product proceeds via dihydride species $[(CAAC)_2Fe(H)_2]$ ($\mathbf{P_{Fe}}$), which then transfers the hydride to carbene carbon, leading to the formation of $\mathbf{Q_{Fe}}$. The formation of $\mathbf{P_{Fe}}$ from catalyst A^{cis}_{Fe} is found to be slightly endergonic (+12.6 kJ/mol) while the formation of $\mathbf{Q_{Fe}}$ is exergonic (−4.5 kJ/mol). Once $\mathbf{Q_{Fe}}$ formation is triggered, the N_2 addition leading to the formation of $[(^{Et}CAAC(H))_2Fe(N2)]$ does not occur, and all attempts to force bind N_2 result in cleavage CAAC ligand, and therefore, the NRR cycle terminates with the formation of $\mathbf{Q_{Fe}}$. $\mathbf{Q_{Fe}}$ acts as a catalytic poison, lowering TON in these reactions, highlighting the need for catalyst design to prioritize reducing hydride intermediate stability over enhancing metal−nitrogen adduct stability in the NRR.

Activation of Nitrogen by $[M(CAAC)_2]$ (where M = Sc−Cu, Pd, Pt, Ad, and Au). As both the mechanism of NH_3 formation and catalytic poisoning steps are established, we have decided to take this further to search for other transition metals that could potentially be better catalysts than Fe. In this regard, we have limited our studies to 13 transition elements Sc, Ti, V, Cr,[32] Mn,[33] Fe,[34] Co,[34−36] Ni,[37] Cu,[38] Pd,[40] Pt,[40] Au,[41,42] and Ag,[41] to which variants of CAAC ligands (with Methyl (^{Me}CAAC), Ethyl (^{Et}CAAC), and cyclohexyl (^{Cy}CAAC) substituents; see Figures 6a and S36) complexation has been reported and experimentally characterized, though for none of the complexes their reactivity toward N_2 has been tested.[96] As a result, we opted to explore variations in ligand architecture in combination with these 13 metal atoms, taking into account both *cis* and trans isomers.

While all 12 metals with the different CAAC ligands were found to yield linear to pseudolinear geometries similar to $[Fe(CAAC)_2]$ reported, Sc was found to yield significant bent geometries with an additional coordination number found to occur via the aryl substituents present in the CAAC architecture (see Figure S37). The electronic structure of linear and low-valent transition metal CAAC complexes, $[M(CAAC)_2]$, reveals that the ligands exhibit redox non-innocence, as evidenced by the $[M^I(CAAC)_2^{\bullet-}]$ configuration. The M−C1 bond length decreases rapidly from 2.3 to 1.8 Å as we move from Sc to Ni, while for Cu, it remains nearly the same as Co metal. This is reflected in the computed ΔE_{int} and ΔE_{orb} energies computed (see Table S39 and Figure S38). The binding mode of the two CAAC ligands, in either *cis* or *trans* fashion, significantly influences the stability of the complexes. For metals such as Ti, V, Mn, Fe, Co, and Ni, the *cis* configuration is consistently more stable, irrespective of the specific CAAC ligand used. In contrast, for Cr, Cu, Ag, and Au, the trans configuration emerges as the ground state, regardless of the CAAC ligand (Figure 6b). This stability trend arises from the weak overlap between the metal d_{xz} orbital and the CAAC π(N−C) orbital in these metals. This weak interaction is reflected in the spin density values, with Cr exhibiting a spin density in the range of 4.6−5.1, while Cu, Ag, and Au show significantly lower spin density values ranging from 0.12−0.16 (see Figures S39−S46). The ∠C1−M−C2 alone explains the 64% variation in the *cis-trans* free energy gap, i.e., ΔG^0_1 (See Figure 6c). The ∠C1−M−C2 angle was found to be in the range of 165−173° for the *cis* isomer of all complexes, with the exception of Ti and V, which have more bent structures. The trans geometries, on the other hand, are in the range of 165−180 ° for all metals (with Ti and V exempted), revealing trans yield linear/pseudolinear geometries compared to the *cis* isomer. Agostic interaction strength can be quantified by M···H bond lengths and follows the order ^{Et}CAAC > ^{Cy}CAAC > ^{Me}CAAC for *cis* isomers of all metals. In contrast, for *trans* isomers, the order is ^{Et}CAAC ∼ ^{Cy}CAAC > ^{Me}CAAC, which is attributed to the reduced bending of the ∠C1−M−C2 angle. The energy difference between *cis* and *trans* isomer (ΔG^0_1) for all geometries, when plotted against the ∠C1−M−C2 angle, reveals that for linear geometries *trans* isomer is found to be stable, while bend geometries lead to stabilization of the *cis* isomer. The ∠C1−M−C2 angle bending increases the buried volume for ^{Et}CAAC compared to those for ^{Cy}CAAC and ^{Me}CAAC ligands in the cis isomer. However, in the trans isomers, the buried volume remains nearly equivalent across all ligands. It is important to note that the buried volume plays a crucial role in N_2 binding. Clearly, ligands and metals that favor *trans* geometries are expected to perform better in NRR reactions. Natural charge analysis indicates that for 4*d*/5d metals, the M−C1 bonds are more ionic compared to 3d metals (see Figures S39−S46).

In the next step, we modeled N_2 binding to all the catalysts, and our calculations reveal that complexes with Ag, Au, Pd, Pt, and Cu metals at their ground state do not bind to N_2 in *cis* and *trans* isomers. In these complexes, ligand charges are found to be larger, indicating a more ionic character. Additionally, the 4*d*/5d orbitals are found to be higher in energy compared to the CAAC π(C−N) orbital, weakening the π-donation/back-donation interactions. The absence of these two critical factors renders these metals ineffective for N_2 binding. The binding energies (ΔG^0_2) for the *cis* isomer increase in a quasi-linear trend as we move from Ti to Ni, whereas the energies for the trans isomer exhibit a zigzag pattern without a clear correlation (see Figures S39−S46). The free energy of the reduction step is closely related to the sum ($\sum q_{cat}$) of the natural charges on the metal center (M) and the atoms C1, C2, N1, and N2 of the CAAC ligands (see Figure 6d). This correlation arises because the reduction process involves electron transfer from the reductant to both the CAAC ligands and the metal. A lower total natural charge results in a lower free energy for the reduction.

In the next step, we modeled the reduction and protonation steps involved in the catalytic cycle, from that, it is clear that the *cis* to *trans* conversion (ΔG^0_1), the binding of dinitrogen to the catalyst (ΔG^0_2), and the one-electron reduction of thduring bond formatione metal−nitrogen adduct (ΔG^0_3) steps were the critical steps (see Tables S40−S45). However, once the first electron is added (as the N≡N bond is broken and the M−N bond is formed), the remaining five electrons and six proton

https://doi.org/10.1021/jacs.5c00099
J. Am. Chem. Soc. 2025, 147, 16948−16963

addition steps (ΔG_4^0 to ΔG_{16}^0) are highly exergonic (more than 100 kJ/mol), suggesting that they proceed rapidly. This suggests that bottleneck steps in this catalytic cycle are the first three steps, and their sum determines the overall efficiency of the catalytic cycle and, consequently, the turnover number (TON). The total free energy, combining all three contributions ($\Delta G_{tot}^0 = \Delta G_1^0 + \Delta G_2^0 + \Delta G_3^0$), represents the total energy cost of N_2 activation; it dictates the overall catalytic efficiency—lower ΔG_{tot}^0 values lead to higher TONs and improved performance, whereas higher values indicate a more energy-demanding and less efficient process. The total free energies (ΔG_{tot}^0) also increase in a quasi-linear fashion for both *cis* and *trans* isomers as the d-orbital occupancy increases (see Figures S39−S46). As shown, multiple factors influence the overall reaction outcome, making a simple mechanistic approach insufficient. Therefore, we turn to machine learning models to uncover design principles for robust catalytic development.

Machine Learning Model. Having understood the scaling relationships, we turned to the integration of machine learning (ML)[97−99] with density functional theory (DFT) calculations, a combination that has proven to greatly enhance catalyst design in recent years.[100] The first step in ML model development is to encode the catalyst structure using specific descriptors.[100] Keeping in this mind, first, we formulated ten different descriptors to represent the catalyst structures, categorized into five groups: (i) geometrical features, including parameters such as C1−M−C2 bond angles, cis-trans isomer, average metal−carbon bond lengths, and ∠N1−C1−N2−C2 torsion angles (F01−F03, F10), (ii) steric attributes, represented by buried volume (F04), (iii) electronic characteristics, encompassing natural charges, d-orbital electron populations, and spin density distributions (F05−F07), (iv) frontier orbital energy levels (F08); (v) noncovalent interaction descriptors, focusing on noncovalent effects such as agostic bonding (F09; see Table S37; see methodologies for more details).

Our approach avoids the complexities associated with optimizing multiple intermediates on the potential energy surface of the nitrogen reduction reaction (NRR), relying instead on initial catalyst calculations. Following this, feature selection is performed to identify the most relevant descriptors. The next steps involve building various models using the selected features and then testing them to evaluate their performance. The final model can then be used to understand and predict catalyst reactivity based on the encoded descriptors. To examine the relationships among the selected descriptors, we computed pairwise Pearson correlation coefficients.[98,101] These correlations, illustrated in Figure 7, reveal the relationships between descriptors and target variables T01 (ΔG_1^0), T02 (ΔG_2^0), T03 (ΔG_3^0), and T04 (ΔG_{tot}). Significant correlations are indicated by high positive or negative values, represented by the light yellow−green or blue colors. This result shows that descriptors such as buried volume (F04) and d-orbital occupation (F07) exhibit strong positive correlations, whereas F03, F05, and F06 exhibit strong negative correlations with the target variable T04, suggesting that these descriptors are highly relevant in explaining the variation in the reaction-free energy (Figure 7).

We explored the impact of these parameters on reaction barriers of NRR by constructing different ML models, where the ΔG_{tot} values were regressed against the parameters. These models allowed us to predict reaction barriers for each data

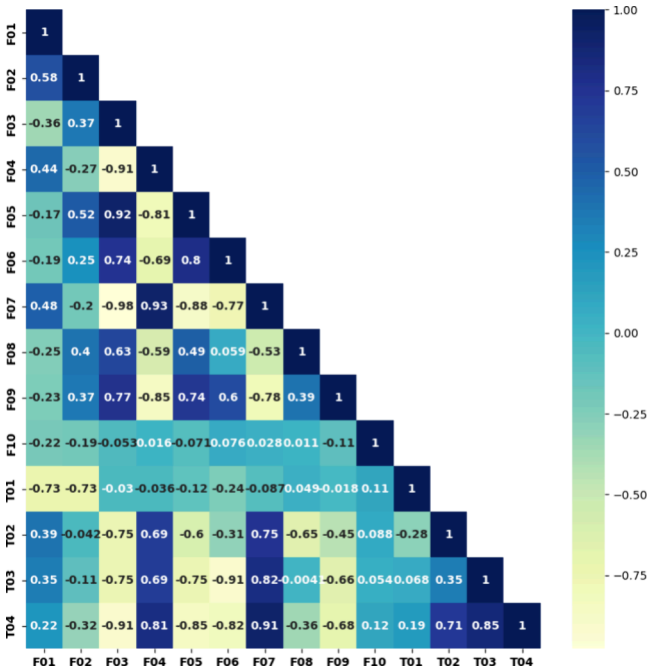

Figure 7. Pairwise correlation matrix between descriptors and target variables. [F01 − θ_{CMC} (∠C1−M−C2), F02 − A_{GS} (isomer ground state), F03 − AVG_{M-C} = (M−C2 + M−C1)/2, M−C1 is bond distance between M and C1, F04 − BV(buried volume), F05 − $\sum\rho_{cat}$ ($\sum\rho_{cat} = \rho_M + \rho_{C1} + \rho_{C2} + \rho_{N1} + \rho_{N2}$) ρ_{C1} is the spin density on 'C1' atom, F06 − $\sum q_{cat}$ ($\sum q_{cat} = q_M + q_{C1} + q_{C2} + q_{N1} + q_{N2}$), q_{C1} is the natural charge on 'C1' atom, F07 − d^n (number of d-electrons), F08 − $\sum E_{FMO}$ ($\sum E_{FMO} = E_{HOMO-1} + E_{HOMO} + E_{LUMO} + E_{LUMO+1}$) E_{HOMO} is energy of HOMO orbital, F09 − Strength of agostic intractions (d_{M-H}), F10 − $\varnothing_{NCNC}$(∠N1−C1−N2-C2), T01 − ΔG_1^0 (ΔG_1^0 free energy of cis-trans isomerization step), T02 − ΔG_2^0 (ΔG_2^0 is free energy of N_2 binding step), and T03 − ΔG_3^0 (ΔG_3^0 is free energy of electron transfer step). T04 − ΔG_{tot}^0($\Delta G_{tot}^0 = \Delta G_1^0 + \Delta G_2^0 + \Delta G_3^0$)].

point, which we then compared with DFT-computed barriers to evaluate the model's effectiveness. We assessed each regression model using several metrics: R^2, leave-one-out (LOO) R^2 (also known as Q^2), and an F-test (see methodology section for details).[102]

Our findings reveal a strong relationship between ΔG_{tot} and F03 (average of the M−C1 and M−C2 distances). Surprisingly, this parameter alone explains 84% of the variation in reaction-free energies within the training set ($R^2 = 0.84$) and demonstrates substantial predictive power (LOO $R^2 = 0.80$; See Tables S46−S50). The ground state spin density parameter (F05) also shows a good correlation ($R^2 = 0.73$), but incorporating this along with the charge parameter (F06) does not significantly improve the performance. In contrast, adding the orbital metric parameter F08 to F03 results in a significant enhancement of the fit. With this combined {F03, F08} model, R^2 increases to 0.91, and LOO R^2 rises to 0.87, indicating both as a good descriptor combination and improved predictive ability (see Figure S47). These improvements are further corroborated by cross-validation scores, which affirm the model performance. A *t*-test for features provides a *p*-value of less than 0.01, suggesting that these improvements are statistically significant. The final model equation is

$$\Delta G_{tot} = 36.17(F08) - 124.25(F03) + 136.70$$

https://doi.org/10.1021/jacs.5c00099
J. Am. Chem. Soc. 2025, 147, 16948−16963

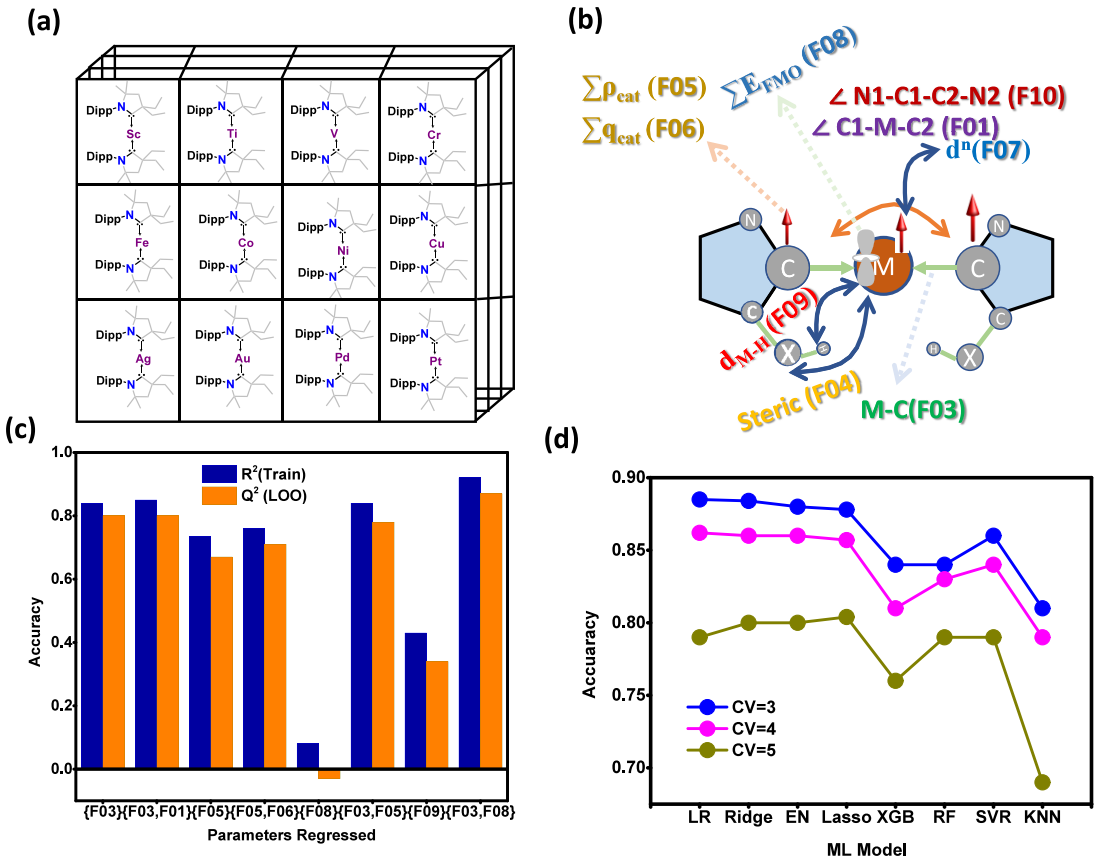

Figure 8. (a) Different complexes used for ML model development (only some are shown), (b) different descriptors employed, (c) statistical results of various multivariate ML models, and (d) Machine learning model performance with the parameters {F03, F08} for the prediction of ΔG^0_{tot}.

The larger coefficient of F03 (average bond length of the M−C bond distance) indicates that ΔG_{tot} is most sensitive to changes in this parameter. This sensitivity stems from the interaction between metal and carbon, which plays a crucial role in the isomerization and N_2 binding steps of NRR. Another parameter, F08 (the energy of frontier molecular orbitals) (FMO), affects electron transfer steps in the nitrogen reduction reaction (NRR). Additionally, various linear models, including Lasso, Ridge, and Elastic Net; nonlinear models, such as XGBoost and random forest; and instance-based methods, such as support vector regression (SVR) and k-nearest neighbors (KNN), were tested. These models demonstrated comparable performance, reinforcing confidence that among the descriptors evaluated, those related to the M−C bond lengths and frontier orbital energies are the most significant parameters influencing NRR. These findings further validate the reliability of the machine learning predictions (see Tables S38−S41).

DISCUSSION

The conversion of N_2 to NH_3 through homogeneous catalysis, achieving exceptional TON and TOF, remains one of the most formidable challenges yet to be overcome by chemists. Among several catalysts with notable performance, the $[(CAAC)_2Fe]$ catalyst stands out due to the versatility of its ligand architecture and the diverse range of metals it can coordinate. This versatility provides an exceptional platform for in-depth computational analysis. Notably, this is the first study of its kind to combine DFT, ab initio molecular dynamics, and ML models to investigate the mechanistic intricacies of N_2 to NH_3 conversion, offering unprecedented insights and laying the groundwork for rational catalyst design.

We initiated our study by modeling the catalytic cycle of $[(CAAC)_2Fe]$ (A^{cis}_{Fe}) reported experimentally. The *cis* isomer (A^{cis}_{Fe}) is found to be more stable than the trans (A^{trans}_{Fe}) by 7.7 kJ/mol, and our calculations revealed that the intermediate spin state (S = 1) of $[(CAAC)_2Fe]$ is the ground state for both isomers. The geometries and energetics are consistent with the experiments, offering confidence in the methodology chosen. The CAAC ligand was found to exhibit redox noninnocence behavior, possessing a net negative spin density of −0.84, suggestive of $[Fe^{I}(CAAC)_2^{\cdot-}]$ as the electronic structures for both isomers. The magnetic coupling between the Fe(I) and the $\{(CAAC)_2^{\cdot-}\}$ radical centers was computed to be strongly antiferromagnetic in nature (J value of -1817 cm^{-1} for A^{cis}_{Fe} and -922 cm^{-1} for A^{trans}_{Fe}) with very strong magnetic coupling noted for A^{cis}_{Fe}due to strong overlap between Fe-(d_{xz}) and CAAC-π(N−C) orbital compared to the A^{trans}_{Fe}(see Figure S48).

We also performed ab initio molecular dynamics on the A_{cis} to understand how binding pockets evolve with time. Our calculations reveal that the bulky Dipp (Dipp = 2,6-diisopropylphenyl) groups stabilize the complex and maintain low-coordinate geometry but exhibit significant fluctuations within 15 ps. These fluctuations, while enhancing stability, impede small molecule access to the metal ions, such as N_2, introducing an energy penalty that limits catalytic efficiency and also rationalizes the temperature-dependent N_2 binding to

https://doi.org/10.1021/jacs.5c00099
J. Am. Chem. Soc. 2025, 147, 16948−16963

$[Fe(CAAC)_2]$ observed in the experiments. In the next step, we explored the full mechanism for N_2-to-NH_3 conversion by $[Fe(CAAC)_2]$, identifying N_2 binding as the crucial first step. The $\boldsymbol{A}_{Fe}^{trans}$ isomer exhibits a lower energy penalty (~30 kJ/mol) compared to that of $\boldsymbol{A}_{Fe}^{cis}$ due to shorter Fe−C bonds and stronger π^* orbital donation from the d_{xz} + Lπ_y orbital of Fe, facilitated by the π-donor CAAC ligands, which elongates the N≡N bond and enhances N_2 activation. In the next step, one electron reduction of the $[(CAAC)_2Fe(N_2)]$ species is triggered. While this is slightly endergonic (17.6 kJ/mol), the reduction was found to occur at the N_2 site, resulting in S = 1/2 ground state with very complex spin density distribution, i.e., $[(CAAC^{\downarrow})^{-}{}_2Fe^{I\uparrow\uparrow\uparrow}(N_2)^{\cdot-\downarrow}]$. This is followed by protonation and further ET-PT steps leading to the formation of ammonia via $[(CAAC)_2Fe{\equiv}N]$ species formation. All the subsequent steps are significantly exergonic, thanks to the $KC_8/HBAr^F{}_4$ combination that eases the overall energetics of the reaction once the N_2 binding completes. The energetics plot reveals that the reaction proceeds downhill throughout the cycle, except for two instances: Fe═N−NH_2 ($\mathbf{F}_{Fe}$) to Fe═N−NH_3 ($\mathbf{G}_{Fe}$) and Fe−NH_2 ($\mathbf{M}_{Fe}$) to Fe−NH_3 ($\mathbf{N}_{Fe}$) conversions. While the catalytic cycle exhibits a high exergonic efficiency, the overall process demands a substantial energy per N_2 to NH_3 conversion. The proton and electron sources (KC_8 and $HBArF_4{\cdot}2Et_2O$ here) compensate for this energy input, enabling the reaction under the given conditions. However, in the absence of such compensation, the energy demand exceeds that of both Haber-Bosch and nitrogenase, highlighting the significant energetic challenges that persist, in general, for molecular NRR catalysts.

The computed energetics reveal efficient conversion of N_2 to NH_3, comparable to those of other reported catalysts. However, the turnover number (TON) is significantly lower, indicating ligand-specific competitive reactions that can interfere with the desired pathway. Specifically, the formation of $[(CAAC(H))_2Fe]$ from $[(CAAC)_2Fe]$ and H_2 (potentially generated from $KC_8/HBAr^F{}_4$) is exothermic by −4.5 kJ/mol and acts as a catalytic poison by limiting N_2 binding. However, the production of H_2 under the experimental conditions is weak, as illustrated by its energetically unfavorable release at the given temperature.[103] Consequently, N_2 binding and subsequent NH_3 conversion remain feasible, although the TON is reduced due to the interplay between temperature-dependent dynamics and competitive inhibition by $[(CAAC(H))_2Fe]$.

After establishing the overall mechanism for nitrogen reduction reactions (NRR) with linear CAAC iron complexes, we broadened our investigation to include a range of transition metals, spanning 3d metals (Sc−Cu) as well as 4d and 5d metals such as Pd, Pt, Ag, and Au (see Figure 8a). Additionally, we have also extended to include various CAAC ligands such as ^{Me}CAAC, ^{Et}CAAC, and ^{Cy}CAAC and their permutation combination, with the objective of employing machine learning (ML) to screen and analyze the key steps identified in the established NRR mechanism. We computed the free energy contributions for key mechanistic steps: *cis*-to-*trans* isomerization ($\boldsymbol{G}_1^0$), N_2 binding to the metal center ($\boldsymbol{\Delta G}_2^0$), and the one-electron reduction of the metal-N_2 adduct ($\boldsymbol{\Delta G}_3^0$).To provide a comprehensive metric, we defined the total free energy parameter as $\boldsymbol{\Delta G_{tot}} = \boldsymbol{\Delta G}_1^0 + \boldsymbol{\Delta G}_2^0 + \boldsymbol{\Delta G}_3^0$, ensuring equal consideration of all these contributions.

In the next step, for encoding the catalyst structures, we have designed ten quantum descriptors that fall broadly into the following five groups: (i) structural parameters (F01−F03, F10 consisting of C1−M−C2, *cis*-trans isomerism, average M−C distance and $\emptyset_{NCNC}\angle$N1−C1−N2−C2) (ii) steric parameters (F04; BV buried volume), (iii) electronic parameters (F05−F07; natural charges, d-electron occupation, and spin densities), (iv) frontier orbital energy parameters (F08) and (v) noncovalent interactions (F09; agostic interactions) (see Figures 8b and 7). Among various ML models that were employed to fit these parameters, the final model that yields an excellent fit to all the data contains essentially two descriptors, i.e., metal−carbon distance (F03) and frontier orbital energy (F08), with the former possessing larger coefficient compared to the latter (see Figure 8c). The significant coefficient of F03, representing the average M−C bond length, highlights that ΔG_{tot} is the most sensitive to changes in this parameter, reflecting its critical role in isomerization and N_2 binding. Additionally, F03, representing the energy of frontier molecular orbitals (FMO), influences electron transfer processes in NRR. The robustness of the model is further confirmed by different cross-validation scores (Figure 8d).

The computed ΔG_{tot} was found to have the following order for the catalyst with various combinations of CAAC ligand tested

$$\begin{aligned}&\text{Ti}\ (24-40\ \text{kJ/mol})\\ &<\text{V}\ (51-60\ \text{kJ/mol})\\ &<\text{Cr}-\text{Fe}\ (73-95\ \text{kJ/mol})\\ &<\text{Mn}-\text{Fe}\ (96-103\ \text{kJ/mol})\\ &<\text{Co}\ (120-129\ \text{kJ/mol})\\ &<\text{Ni}\ (147-157\ \text{kJ/mol})\end{aligned}$$

Clearly, this order suggests that with all different variations of the CAAC ligand, $[Ti(CAAC)_2]$ performs the best in all metrics, yielding the lowest energy penalty for all three ΔG parameters. While complexation with $[Ti(CAAC)_2Cl_3]$ and $[Ti(CAAC)_2Cl_4]$ was reported, a zerovalent state has not been reported and can be targeted for potential NRR reactivity.[104,105] This is followed by V complexes with a slightly higher energy penalty, and this is followed by Cr, Fe, and Mn, which possess energy in the order of 75−100 kJ/mol. Late transition metal ions such as Co and Ni were found to have even higher energy penalties, irrespective of the ligand modifications, while coinage metals failed to bind to nitrogen. The observed order of ΔG_{tot} for the $[M(CAAC)_2]$ catalysts reflects a balance of d-orbital occupancy, ligand effects, and back-donation efficiency to the π^* orbital of N_2. Early transition metals like Ti and V exhibit the lowest energy penalties due to their accessible d-orbitals, low π-Lewis acidity, and the noninnocent CAAC ligands, which enhance electron transfer and stabilize the zerovalent state. In contrast, late transition and coinage metals, with nearly filled or energetically mismatched d-orbitals, show poor back-donation and higher energy penalties, limiting their ability to bind and activate N_2 effectively.

Overall, earlier experimental studies have established key catalytic trends, such as temperature-dependent N_2 binding and turnover limitations; however, the mechanistic origins of these observations remained unclear. Our study systematically addresses these gaps through a combination of DFT, AIMD, and ML, providing a first-principles rationale for these

https://doi.org/10.1021/jacs.5c00099
J. Am. Chem. Soc. 2025, 147, 16948−16963

experimentally observed behaviors. We reveal that dynamic steric fluctuations of bulky Dipp groups introduce an energy penalty on N_2 coordination, partially explaining the experimental temperature dependence of reactivity. Furthermore, we identify a previously unrecognized catalytic deactivation pathway, where $[(CAAC(H))_2Fe]$ formation acts as a competitive sink that limits TON despite weak H_2 formation under experimental conditions. By systematically investigating a range of transition metals, we computationally establish a quantitative reactivity order, demonstrating that early transition metals (Ti, V) outperform late transition metals (Co, Ni) due to stronger π-back-donation. Our ML analysis further highlights M−C bond length (F03) and frontier orbital energy (F08) as the primary descriptors governing N_2 activation efficiency, bridging experimental findings with a predictive catalyst design framework. While this study establishes a predictive ML framework for catalyst screening in low-valent transition metal-mediated NRR, future advancements could enhance its applicability by expanding the training set to diverse ligand classes and experimental data, which could further refine catalyst design. The insights gained lay the groundwork for advancing homogeneous catalysts capable of efficient and scalable NRR, driving progress in sustainable ammonia production.

CONCLUSIONS

The conversion of N_2 to NH_3 under ambient conditions remains one of the greatest unsolved chemical challenges of this century, with immense industrial relevance, as ammonia production drives a global market exceeding $70 billion annually. The development of a robust homogeneous catalyst that can efficiently perform this task with a higher turnover number has been ongoing research with 3*d*/4d/5d metals over the years and has shown some prominence. Building on these advancements and leveraging the capabilities of robust ML models for analyzing large data sets, screening, and prediction, we address this challenge in the present work using a combination of DFT, ab initio molecular dynamics, and ML tools. The conclusions derived are summarized below.

Ligand Architecture a Double-Edged Sword? We have modeled the NRR reaction catalyzed by $[Fe(CAAC)_2]$, uncovering spin leakage from the CAAC ligand to the metal, indicative of strong redox noninnocence with $[M^I(CAAC)_2^{\cdot-}]$ electronic ground state with strong antiferromagnetic coupling between the metal and the $(CAAC)_2^{\cdot-}$ ligand. This noninnocent behavior is identified as crucial for stabilizing low-valent metal ions. The *cis-trans* isomerization, dinitrogen binding, and reduction of the dinitrogen complex emerge as the most energetically challenging steps, with subsequent transformations leading to two equivalents of NH_3 being highly exothermic. While the CAAC → Metal → $\pi^*(N_2)$ electron donation pathway is essential for N_2 binding, ab initio molecular dynamics simulations reveal that the bulky ligand decorations hinder the metal's accessibility to N_2. Moreover, the CAAC ligands, while stabilizing the $[(CAAC)_2M(N_2)]$, favor the exothermic formation of $\{(CAAC(H))_2M\}$ under reaction conditions, poisoning the catalytic cycle and presenting a double-edged sword.

Data-Driven Approaches for NRR Catalyst Design Using Machine Learning. We then expanded our studies to include other linear, low-valent transition metal CAAC complexes, exploring combinations of Sc-Cu, Ag, Au, Pd, and Pt while also varying the substituents on the CAAC ligand. While the redox noninnocence was found to persist in all cases, the binding mode of the two CAAC ligands, either in *cis* or trans fashion, significantly influences the stability of the complexes. The *cis* isomer is consistently more stable for metals such as Ti, V, Mn, Fe, Co, and Ni, irrespective of the specific CAAC ligand used. In contrast, for Cr, Cu, Ag, and Au, the *trans* isomer emerges as the ground state regardless of the CAAC ligand, which is attributed to weaker metal-CAAC interactions. Armed with all the data, we have screened more than ten quantum descriptors based on structural, electronic, and steric factors associated with free catalysts and several ML models. Analyzing various factors such as metal type, spin state, steric environment, ligand radical character, and orbital effects reveals that the average M−C bond length and the energy of frontier molecular orbitals are the most significant parameters influencing NRR. Our study predicts that $[Ti(CAAC)_2]$ catalysts exhibit the lowest energy penalties for key NRR mechanistic steps, attributed to their accessible d-orbitals that align well with the CAAC frontier molecular orbitals, low π-Lewis acidity, and redox-active CAAC ligands. Vanadium complexes follow closely, while Cr, Fe, and Mn show moderate energy penalties, balancing effective orbital overlap and electron transfer. In contrast, late transition and coinage metals such as Co, Ni, Ag, and Au exhibit higher energy penalties due to poorly aligned d-orbitals and limited back-donation efficiency, restricting effective N_2 activation.

To this end, this work combines state-of-the-art quantum chemistry with machine learning tools for the first time to solve the outstanding issues in the area of nitrogen reduction, setting the stage for new catalysts design for the sustainable production of ammonia.

ASSOCIATED CONTENT

Data Availability Statement

The code and data are available through the GitHub link (https://github.com/gopalan-rajaraman/CAAC_TM_Nitrogen).

Supporting Information

The Supporting Information is available free of charge at https://pubs.acs.org/doi/10.1021/jacs.5c00099.

Structural and NBO analysis of different spin states (Figures S1, S2 and Tables S1−S6); ab initio molecular dynamics results (Figure S7); geometries and spin density plots of intermediates involved in NRR and catalytic poisoning steps (Figures S8−S35 and Tables S7−S38); interaction energies of various complexes (Table S39); energetics of NRR intermediates for different metals (Tables S40−S45); plots of catalytic activity changes across different complexes and descriptors (Figures S36−S46); ML model performance (Figure S47); descriptor data, ML models, and accuracy evaluations (Tables S46−S50); and variation in orbital interaction in cis and trans isomers (Figure S48) (PDF)

AUTHOR INFORMATION

Corresponding Author

Gopalan Rajaraman − *Department of Chemistry, Indian Institute of Technology Bombay, Mumbai 400076, India;* orcid.org/0000-0001-6133-3026; Email: rajaraman@chem.iitb.ac.in

https://doi.org/10.1021/jacs.5c00099
J. Am. Chem. Soc. 2025, 147, 16948−16963

Authors

Chandrasekhar Nettem − *Department of Chemistry, Indian Institute of Technology Bombay, Mumbai 400076, India*

Ankit Mondal − *Department of Chemistry, Indian Institute of Technology Bombay, Mumbai 400076, India*

Complete contact information is available at: https://pubs.acs.org/10.1021/jacs.5c00099

Notes

The authors declare no competing financial interest.

■ ACKNOWLEDGMENTS

CSN thanks IIT Bombay for the fellowship and HPC facility. GR would like to thank SERB (SB/SJF/2019-20/12; CRG/2022/001697) for funding.

■ REFERENCES

(1) Spatolisano, E.; Pellegrini, L. A.; de Angelis, A. R.; Cattaneo, S.; Roccaro, E. Ammonia as a Carbon-Free Energy Carrier: NH3 Cracking to H2. *Ind. Eng. Chem. Res.* **2023**, *62* (28), 10813−10827.

(2) Huang, X.; Du, R.; Ren, J.; Li, X.; Fu, M.; Fu, S.; Ma, T.; Guo, L.; Soomro, R. A.; Yang, C.; Wang, D. Unveiling the Mechanism of Aerobic Photocatalytic Nitrogen Fixation over Dynamic Structural Renovation on Bi2MO6 (M = Mo, W). *ACS Catal.* **2024**, *14* (18), 13542−13549.

(3) Li, S.; Zhou, Y.; Fu, X.; Pedersen, J. B.; Saccoccio, M.; Andersen, S. Z.; Enemark-Rasmussen, K.; Kempen, P. J.; Damsgaard, C. D.; Xu, A.; Sažinas, R.; Mygind, J. B. V.; Deissler, N. H.; Kibsgaard, J.; Vesborg, P. C. K.; Nørskov, J. K.; Chorkendorff, I. Long-term continuous ammonia electrosynthesis. *Nature* **2024**, *629* (8010), 92−97.

(4) Högbom, M. A dynamic tool for nitrogen reduction. *Science* **2014**, *345* (6204), 1568−1568.

(5) Peters, J. W.; Einsle, O.; Dean, D. R.; DeBeer, S.; Hoffman, B. M.; Holland, P. L.; Seefeldt, L. C. Comment on "Structural evidence for a dynamic metallocofactor during N2 reduction by Mo-nitrogenase". *Science* **2021**, *371* (6530), No. eabe5481.

(6) Kang, W.; Lee, C. C.; Jasniewski, A. J.; Ribbe, M. W.; Hu, Y. Structural evidence for a dynamic metallocofactor during N2 reduction by Mo-nitrogenase. *Science* **2020**, *368* (6497), 1381−1385.

(7) Schlögl, R. Ammonia Iron: An Epistemic Challenge with Practical Consequences. *J. Phys. Chem. C* **2024**, *128* (46), 19601−19620.

(8) Crossland, J. L.; Tyler, D. R. Iron−dinitrogen coordination chemistry: dinitrogen activation and reactivity. *Coord. Chem. Rev.* **2010**, *254* (17−18), 1883−1894.

(9) Chalkley, M. J.; Drover, M. W.; Peters, J. C. Catalytic N2-to-NH3 (or-N2H4) conversion by well-defined molecular coordination complexes. *Chem. Rev.* **2020**, *120* (12), 5582−5636.

(10) Anderson, J. S.; Rittle, J.; Peters, J. C. Catalytic conversion of nitrogen to ammonia by an iron model complex. *Nature.* **2013**, *501* (7465), 84−87.

(11) Tanabe, Y.; Nishibayashi, Y. Developing more sustainable processes for ammonia synthesis. *Coord. Chem. Rev.* **2013**, *257* (17−18), 2551−2564.

(12) Schlögl, R. Catalytic synthesis of ammonia—a "never-ending story"? *Angew. Chem., Int. Ed.* **2003**, *42* (18), 2004−2008.

(13) Tanaka, H.; Nishibayashi, Y.; Yoshizawa, K. Interplay between theory and experiment for ammonia synthesis catalyzed by transition metal complexes. *Acc. Chem. Res.* **2016**, *49* (5), 987−995.

(14) Tanabe, Y.; Nishibayashi, Y. Comprehensive insights into synthetic nitrogen fixation assisted by molecular catalysts under ambient or mild conditions. *Chem. Soc. Rev.* **2021**, *50* (8), 5201−5242.

(15) Mateo, D.; Sousa, A.; Zakharzhevskii, M.; Gascon, J. Challenges and opportunities for the photo-(thermal) synthesis of ammonia. *Green Chem.* **2024**, *26* (3), 1041−1061.

(16) Shahed Gharahshiran, V.; Zheng, Y. Sustainable ammonia synthesis: An in-depth review of non-thermal plasma technologies. *J. Energy Chem.* **2024**, *96*, 1−38.

(17) Nadiri, S.; Attari Moghaddam, A.; Folke, J.; Ruland, H.; Shu, B.; Fernandes, R.; Schlögl, R.; Krewer, U. Ammonia synthesis rate over a wide operating range: from experiments to validated kinetic models. *ChemCatChem* **2024**, *16* (23), No. e202400890.

(18) Shen, H.; Choi, C.; Masa, J.; Li, X.; Qiu, J.; Jung, Y.; Sun, Z. Electrochemical ammonia synthesis: Mechanistic understanding and catalyst design. *Chem.* **2021**, *7* (7), 1708−1754.

(19) Nawaz, M. A.; Blay-Roger, R.; Saif, M.; Meng, F.; González-Arias, J.; Miao, B.; Bobadilla, L. F.; Ramirez-Reina, T.; Odriozola, J. A. Enroute to the Carbon-Neutrality Goals via the Targeted Development of Ammonia as a Potential Nitrogen-Based Energy Carrier. *ACS Catal.* **2023**, *13* (21), 14415−14453.

(20) Levi, P. G.; Cullen, J. M. Mapping global flows of chemicals: from fossil fuel feedstocks to chemical products. *Environ. Sci. Technol.* **2018**, *52* (4), 1725−1734.

(21) Vinardell, S.; Nicolas, P.; Sastre, A. M.; Cortina, J. L.; Valderrama, C. Sustainability Assessment of Green Ammonia Production To Promote Industrial Decarbonization in Spain. *ACS Sustain Chem. Eng.* **2023**, *11* (44), 15975−15983.

(22) Roux, Y.; Duboc, C.; Gennari, M. Molecular catalysts for N2 reduction: state of the art, mechanism, and challenges. *ChemPhysChem* **2017**, *18* (19), 2606−2617.

(23) Van der Ham, C. J.; Koper, M. T.; Hetterscheid, D. G. Challenges in reduction of dinitrogen by proton and electron transfer. *Chem. Soc. Rev.* **2014**, *43* (15), 5183−5191.

(24) Yang, J.; Xie, X.; Wang, X.; Dixon, R.; Wang, Y.-P. Reconstruction and minimal gene requirements for the alternative iron-only nitrogenase in Escherichia coli. *Proc. Natl. Acad. Sci.* **2014**, *111* (35), E3718−E3725.

(25) Hoffman, B. M.; Lukoyanov, D.; Yang, Z.-Y.; Dean, D. R.; Seefeldt, L. C. Mechanism of Nitrogen Fixation by Nitrogenase: The Next Stage. *Chem. Rev.* **2014**, *114* (8), 4041−4062.

(26) Burgess, B. K.; Lowe, D. J. Mechanism of Molybdenum Nitrogenase. *Chem. Rev.* **1996**, *96* (7), 2983−3012.

(27) Smith, C.; Hill, A. K.; Torrente-Murciano, L. Current and future role of Haber−Bosch ammonia in a carbon-free energy landscape. *Energy Environ. Sci.* **2020**, *13* (2), 331−344.

(28) Einsle, O.; Rees, D. C. Structural enzymology of nitrogenase enzymes. *Chem. Rev.* **2020**, *120* (12), 4969−5004.

(29) Yandulov, D. V.; Schrock, R. R. Catalytic Reduction of Dinitrogen to Ammonia at a Single Molybdenum Center. *Science* **2003**, *301* (5629), 76−78.

(30) Taylor, L. J.; Kays, D. L. Low-coordinate first-row transition metal complexes in catalysis and small molecule activation. *Dalton Trans.* **2019**, *48* (33), 12365−12381.

(31) Ung, G.; Peters, J. C. Low-Temperature N2 Binding to Two-Coordinate L2Fe0 Enables Reductive Trapping of L2FeN2−and NH3 Generation. *Angew. Chem., Int. Ed.* **2015**, *54* (2), 532−535.

(32) Samuel, P. P.; Neufeld, R.; Mondal, K. C.; Roesky, H. W.; Herbst-Irmer, R.; Stalke, D.; Demeshko, S.; Meyer, F.; Rojisha, V. C.; De, S.; et al. Cr (I) Cl as well as Cr+ are stabilised between two cyclic alkyl amino carbenes. *Chem. Sci.* **2015**, *6* (5), 3148−3153.

(33) Samuel, P. P.; Mondal, K. C.; Roesky, H. W.; Hermann, M.; Frenking, G.; Demeshko, S.; Meyer, F.; Stückl, A. C.; Christian, J. H.; Dalal, N. S.; et al. Synthesis and Characterization of a Two-Coordinate Manganese Complex and its Reaction with Molecular Hydrogen at Room Temperature. *Angew. Chem., Int. Ed.* **2013**, *52* (45), 11817−11821.

(34) Ung, G.; Rittle, J.; Soleilhavoup, M.; Bertrand, G.; Peters, J. C. Two-Coordinate Fe0 and Co0 Complexes Supported by Cyclic (alkyl)(amino) carbenes. *Angew. Chem., Int. Ed.* **2014**, *53* (32), 8427−8431.

(35) Mondal, K. C.; Roy, S.; De, S.; Parameswaran, P.; Dittrich, B.; Ehret, F.; Kaim, W.; Roesky, H. W. Stabilization of a Two-Coordinate Mononuclear Cobalt (0) Compound. *Chem. − Eur. J.* **2014**, *20* (37), 11646−11649.

(36) Du, J.; Chen, W.; Chen, Q.; Leng, X.; Meng, Y.-S.; Gao, S.; Deng, L. Reactivity of a two-coordinate cobalt (0) cyclic (alkyl)-(amino) carbene complex. *Organometallics.* **2020**, *39* (5), 729−739.
(37) Mondal, K. C.; Samuel, P. P.; Li, Y.; Roesky, H. W.; Roy, S.; Ackermann, L.; Sidhu, N. S.; Sheldrick, G. M.; Carl, E.; Demeshko, S.; et al. A Catalyst with Two-Coordinate Nickel: Theoretical and Catalytic Studies. *Eur. J. Inorg. Chem.* **2014**, *2014* (5), 818−823.
(38) Weinberger, D. S.; Amin, S. K. N.; Mondal, K. C.; Melaimi, M.; Bertrand, G.; Stückl, A. C.; Roesky, H. W.; Dittrich, B.; Demeshko, S.; Schwederski, B.; et al. Isolation of neutral mononuclear copper complexes stabilized by two cyclic (alkyl)(amino) carbenes. *J. Am. Chem. Soc.* **2014**, *136* (17), 6235−6238.
(39) Singh, A. P.; Samuel, P. P.; Roesky, H. W.; Schwarzer, M. C.; Frenking, G.; Sidhu, N. S.; Dittrich, B. A singlet biradicaloid zinc compound and its nonradical counterpart. *J. Am. Chem. Soc.* **2013**, *135* (19), 7324−7329.
(40) Roy, S.; Mondal, K. C.; Meyer, J.; Niepötter, B.; Köhler, C.; Herbst-Irmer, R.; Stalke, D.; Dittrich, B.; Andrada, D. M.; Frenking, G.; et al. Synthesis, Characterization, and Theoretical Investigation of Two-Coordinate Palladium (0) and Platinum (0) Complexes Utilizing π-Accepting Carbenes. *Chem. − Eur. J.* **2015**, *21* (26), 9312−9318.
(41) Jerabek, P.; Roesky, H. W.; Bertrand, G.; Frenking, G. Coinage metals binding as main group elements: structure and bonding of the carbene complexes [TM (cAAC) 2] and [TM (cAAC) 2]+(TM= Cu, Ag, Au). *J. Am. Chem. Soc.* **2014**, *136* (49), 17123−17135.
(42) Weinberger, D. S.; Melaimi, M.; Moore, C. E.; Rheingold, A. L.; Frenking, G.; Jerabek, P.; Bertrand, G. Isolation of neutral mono-and dinuclear gold complexes of cyclic (alkyl)(amino) carbenes. *Angew. Chem., Int. Ed.* **2013**, *52* (34), 8964−8967.
(43) Mariano, L. A.; Nguyen, V. H. A.; Briganti, V.; Lunghi, A. Charting Regions of Cobalt's Chemical Space with Maximally Large Magnetic Anisotropy: A Computational High-Throughput Study. *J. Am. Chem. Soc.* **2024**, *146* (49), 34158−34166.
(44) Nguyen, V. H. A.; Lunghi, A. Predicting tensorial molecular properties with equivariant machine learning models. *Phys. Rev. B* **2022**, *105* (16), No. 165131.
(45) Lunghi, A.; Sanvito, S. Computational design of magnetic molecules and their environment using quantum chemistry, machine learning and multiscale simulations. *Nat. Rev. Chem.* **2022**, *6* (11), 761−781.
(46) Zhang, S.; Lu, S.; Zhang, P.; Tian, J.; Shi, L.; Ling, C.; Zhou, Q.; Wang, J. Accelerated discovery of single-atom catalysts for nitrogen fixation via machine learning. *Energy Environ. Mater.* **2023**, *6* (1), No. e12304.
(47) Mou, T.; Pillai, H. S.; Wang, S.; Wan, M.; Han, X.; Schweitzer, N. M.; Che, F.; Xin, H. Bridging the complexity gap in computational heterogeneous catalysis with machine learning. *Nat. Catal.* **2023**, *6* (2), 122−136.
(48) Wang, X.; Jiang, S.; Hu, W.; Ye, S.; Wang, T.; Wu, F.; Yang, L.; Li, X.; Zhang, G.; Chen, X.; et al. Quantitatively determining surface−adsorbate properties from vibrational spectroscopy with interpretable machine learning. *J. Am. Chem. Soc.* **2022**, *144* (35), 16069−16076.
(49) Wang, X.; Shi, K.; Peng, A.; Snurr, R. Q. Computational Chemistry and Machine Learning-Assisted Screening of Supported Amorphous Metal Oxide Nanoclusters for Methane Activation. *ACS Catal.* **2024**, *14* (24), 18708−18721.
(50) Becke, A. D. Density-functional thermochemistry. V. Systematic optimization of exchange-correlation functionals. *J. Chem. Phys.* **1997**, *107* (20), 8554−8560.
(51) Becke, A. D. Density-functional exchange-energy approximation with correct asymptotic behavior. *Phys. Rev. A* **1988**, *38* (6), 3098.
(52) Antony, J.; Grimme, S. Density functional theory including dispersion corrections for intermolecular interactions in a large benchmark set of biologically relevant molecules. *Phys. Chem. Chem. Phys.* **2006**, *8* (45), 5287−5293.
(53) Dey, S.; Nettem, C. S.; Rajaraman, G.; Ghosh, P. Convenient access to amidines by mesoionic singlet palladium carbene catalyzed hydrazone-isocyanide-amine (HIA) coupling: Scope and mechanistic insights. *Mol. Catal.* **2024**, *553*, No. 113735.
(54) Kumar, A.; Ta, S.; Nettem, C.; Tanski, J. M.; Rajaraman, G.; Ghosh, P. One pot tandem dehydrogenative cross-coupling of primary and secondary alcohols by ruthenium amido-functionalized 1, 2, 4-triazole derived N-heterocyclic carbene complexes. *RSC Adv.* **2022**, *12* (45), 28961−28984.
(55) Hay, P. J.; Wadt, W. R. Ab initio effective core potentials for molecular calculations. Potentials for the transition metal atoms Sc to Hg. *J. Chem. Phys.* **1985**, *82* (1), 270−283.
(56) Hay, P. J.; Wadt, W. R. Ab initio effective core potentials for molecular calculations. Potentials for K to Au including the outermost core orbitals. *J. Chem. Phys.* **1985**, *82* (1), 299−310.
(57) Frisch, M.; Trucks, G.; Schlegel, H.; Scuseria, G.; Robb, M.; Cheeseman, J.; Scalmani, G.; Barone, V.; Mennucci, B.; Petersson, G.*Gaussian 09*; Gaussian, Inc.: Wallingford, CT, 2009; Vol. *32*, pp 5648−5652.
(58) Lu, T.; Chen, F. Multiwfn: a multifunctional wavefunction analyzer. *J. Comput. Chem.* **2012**, *33* (5), 580−592.
(59) Prakasham, A. P.; Patil, S. K.; Nettem, C.; Dey, S.; Rajaraman, G.; Ghosh, P. Discrete Singular Metallophilic Interaction in Stable Large 12-Membered Binuclear Silver and Gold Metallamacrocycles of Amido-Functionalized Imidazole and 1,2,4-Triazole-Derived N-Heterocyclic Carbenes. *ACS Omega* **2023**, *8* (7), 6439−6454.
(60) Luchini, G.; Paton, R., DBSTEP: DFT Based Steric Parameters, 2022. .
(61) Andersson, K.; Malmqvist, P. Å.; Roos, B. O. Second-order perturbation theory with a complete active space self-consistent field reference function. *J. Chem. Phys.* **1992**, *96* (2), 1218−1226.
(62) Malmqvist, P. Å.; Rendell, A.; Roos, B. O. The restricted active space self-consistent-field method, implemented with a split graph unitary group approach. *J. Phys. Chem.* **1990**, *94* (14), 5477−5482.
(63) Sarkar, A.; Gagliardi, L. Multiconfiguration Pair-Density Functional Theory for Vertical Excitation Energies in Actinide Molecules. *J. Phys. Chem. A* **2023**, *127* (44), 9389−9397.
(64) Neese, F. The ORCA program system. *Wiley Interdiscip. Rev. Comput. Mol. Sci.* **2012**, *2* (1), 73−78.
(65) Neese, F. Software update: the ORCA program system, version 4.0. *Wiley Interdiscip. Rev.: Comput. Mol. Sci.* **2018**, *8* (1), No. e1327.
(66) Neese, F. Software update: The ORCA program system—Version 5.0. *Wiley Interdiscip. Rev.: Comput. Mol. Sci.* **2022**, *12* (5), No. e1606.
(67) Lenthe, E. v.; Baerends, E.-J.; Snijders, J. G. Relativistic regular two-component Hamiltonians. *J. Chem. Phys.* **1993**, *99* (6), 4597−4610.
(68) Sen, A.; Ansari, A.; Swain, A.; Pandey, B.; Rajaraman, G. Probing the Origins of Puzzling Reactivity in Fe/Mn−Oxo/Hydroxo Species toward C−H Bonds: A DFT and Ab Initio Perspective. *Inorg. Chem.* **2023**, *62* (37), 14931−14941.
(69) Neale, S. E.; Pantazis, D. A.; Macgregor, S. A. Accurate computed spin-state energetics for Co(iii) complexes: implications for modelling homogeneous catalysis. *Dalton Trans.* **2020**, *49* (19), 6478−6487.
(70) Neese, F.; Wennmohs, F.; Becker, U.; Riplinger, C. The ORCA quantum chemistry program package. *J. Chem. Phys.* **2020**, *152* (22), 224108.
(71) Hutter, J.; Iannuzzi, M.; Schiffmann, F.; VandeVondele, J. cp2k: atomistic simulations of condensed matter systems. *Wiley Interdiscip. Rev. Comput. Mol. Sci.* **2014**, *4* (1), 15−25.
(72) VandeVondele, J.; Krack, M.; Mohamed, F.; Parrinello, M.; Chassaing, T.; Hutter, J. Quickstep: Fast and accurate density functional calculations using a mixed Gaussian and plane waves approach. *Comput. Phys. Commun.* **2005**, *167* (2), 103−128.
(73) Perdew, J. P.; Burke, K.; Ernzerhof, M. Perdew, burke, and ernzerhof reply. *Phys. Rev. Lett.* **1998**, *80* (4), 891.
(74) Sharma, T.; Singh, M. K.; Gupta, R.; Khatua, M.; Rajaraman, G. In silico design to enhance the barrier height for magnetization reversal in Dy(iii) sandwich complexes by stitching them under the umbrella of corannulene. *Chem. Sci.* **2021**, *12* (34), 11506−11514.

https://doi.org/10.1021/jacs.5c00099
J. Am. Chem. Soc. 2025, 147, 16948−16963

(75) Humphrey, W.; Dalke, A.; Schulten, K. VMD: visual molecular dynamics. *J. Mol. Graph.* **1996**, *14* (1), 33−38.
(76) Hartwigsen, C.; Goedecker, S.; Hutter, J. Electronic structure: Wide-band, narrow-band, and strongly correlated systems-Relativistic separable dual-space Gaussian pseudopotentials from H to Rn. *Phys. Rev. B Condens. Matter* **1998**, *58* (7), 3641−3662.
(77) Freund, Y.; Schapire, R. E. A decision-theoretic generalization of on-line learning and an application to boosting. *J. Comput. Syst. Sci.* **1997**, *55* (1), 119−139.
(78) Breiman, L. Random forests. *Mach. Learn.* **2001**, *45*, 5−32.
(79) Chen, T.; Guestrin, C. A scalable tree boosting system. In *Proceedings of the 22nd ACM SIGKDD International Conference on Knowledge Discovery and Data Mining*; Association for Computing Machinery: New York, 2016; pp 785−794.
(80) Zhong, S.; Zhang, K.; Wang, D.; Zhang, H. Shedding light on "Black Box" machine learning models for predicting the reactivity of HO radicals toward organic compounds. *Chem. Eng. J.* **2021**, *405*, No. 126627.
(81) Xu, W.; Long, F.; Zhao, H.; Zhang, Y.; Liang, D.; Wang, L.; Lesnik, K. L.; Cao, H.; Zhang, Y.; Liu, H. Performance prediction of ZVI-based anaerobic digestion reactor using machine learning algorithms. *Waste Manag.* **2021**, *121*, 59−66.
(82) Schneider, J. E.; Goetz, M. K.; Anderson, J. S. Statistical analysis of C−H activation by oxo complexes supports diverse thermodynamic control over reactivity. *Chem. Sci.* **2021**, *12* (11), 4173−4183.
(83) Yelle, R. B.; Crossland, J. L.; Szymczak, N. K.; Tyler, D. R. Theoretical studies of N2 reduction to ammonia in Fe (dmpe) 2N2. *Inorg. Chem.* **2009**, *48* (3), 861−871.
(84) Studt, F.; Tuczek, F. Energetics and Mechanism of a Room-Temperature Catalytic Process for Ammonia Synthesis (Schrock Cycle): Comparison with Biological Nitrogen Fixation. *Angew. Chem., Int. Ed.* **2005**, *44* (35), 5639−5642.
(85) Zadrozny, J. M.; Xiao, D. J.; Atanasov, M.; Long, G. J.; Grandjean, F.; Neese, F.; Long, J. R. Magnetic blocking in a linear iron (I) complex. *Nat. Chem.* **2013**, *5* (7), 577−581.
(86) Brookhart, M.; Green, M. L.; Parkin, G. Agostic interactions in transition metal compounds. *Proc. Natl. Acad. Sci.* **2007**, *104* (17), 6908−6914.
(87) Huzan, M. S.; Burrow, T. G.; Fix, M.; Breitner, F. A.; Chong, S. K.; Bencok, P.; Aramini, M.; Jesche, A.; Baker, M. L. Quantifying the influence of 3d−4s mixing on linearly coordinated metal-ions by L 2, 3-edge XAS and XMCD. *Chem. Sci.* **2024**, *15* (7), 2433−2442.
(88) Ortuno, M. A.; Vidossich, P.; Ujaque, G.; Conejero, S.; Lledos, A. Solution dynamics of agostic interactions in T-shaped Pt (II) complexes from ab initio molecular dynamics simulations. *Dalton Trans.* **2013**, *42* (34), 12165−12172.
(89) Vermeeren, P.; van der Lubbe, S. C.; Fonseca Guerra, C.; Bickelhaupt, F. M.; Hamlin, T. A. Understanding chemical reactivity using the activation strain model. *Nat. Protoc.* **2020**, *15* (2), 649−667.
(90) Clavier, H.; Nolan, S. P. Percent buried volume for phosphine and N-heterocyclic carbene ligands: steric properties in organometallic chemistry. *Chem. Commun.* **2010**, *46* (6), 841−861.
(91) Kfoury, J.; Oláh, J. Role of Lewis acid/base anchor atoms in catalyst regeneration: a comprehensive study on biomimetic EP 3 Fe nitrogenases. *Phys. Chem. Chem. Phys.* **2024**, *26* (16), 12520−12529.
(92) Jiang, W.; DeYonker, N. J.; Wilson, A. K. Multireference character for 3d transition-metal-containing molecules. *J. Chem. Theory Comput.* **2012**, *8* (2), 460−468.
(93) Lyaskovskyy, V.; de Bruin, B. Redox Non-Innocent Ligands: Versatile New Tools to Control Catalytic Reactions. *ACS Catal.* **2012**, *2* (2), 270−279.
(94) Siddiqui, S. A.; Stuyver, T.; Shaik, S.; Dubey, K. D. Designed Local Electric Fields— Promising Tools for Enzyme Engineering. *JACS Au.* **2023**, *3* (12), 3259−3269.
(95) Kuriyama, S.; Nishibayashi, Y., Catalytic Transformations of Molecular Dinitrogen by Iron and Cobalt−Dinitrogen Complexes as Catalysts. In *Nitrogen Fixation*, Nishibayashi, Y., Ed. Springer International Publishing: Cham, 2017; pp 215−234.
(96) Roy, S.; Mondal, K. C.; Roesky, H. W. Cyclic Alkyl(amino) Carbene Stabilized Complexes with Low Coordinate Metals of Enduring Nature. *Acc. Chem. Res.* **2016**, *49* (3), 357−369.
(97) Yang, W.; Fidelis, T. T.; Sun, W.-H. Machine learning in catalysis, from proposal to practicing. *ACS Omega* **2020**, *5* (1), 83−88.
(98) Nettem, C.; Rajaraman, G. How do quantum chemical descriptors shape hydrogen atom abstraction reactivity in cupric-superoxo species? A combined DFT and machine learning perspective. *Inorg. Chem. Front.* **2024**, *11*, 3830−3846.
(99) Butler, K. T.; Davies, D. W.; Cartwright, H.; Isayev, O.; Walsh, A. Machine learning for molecular and materials science. *Nature.* **2018**, *559* (7715), 547−555.
(100) Yang, X.; Dang, J.; Zhang, C.; Li, J.; Niu, S.; Gao, H.; Liu, B.; Guo, Z.; Ma, H. Comparing the Catalytic Effect of Metals for Energetic Materials: Machine Learning Prediction of Adsorption Energies on Metals. *Langmuir.* **2024**, *40* (1), 1087−1095.
(101) Gravier, J.; Vignal, V.; Bissey-Breton, S.; Farre, J. The use of linear regression methods and Pearson's correlation matrix to identify mechanical−physical−chemical parameters controlling the micro-electrochemical behaviour of machined copper. *Corros. Sci.* **2008**, *50* (10), 2885−2894.
(102) Freedman, D. A. *Statistical models: theory and practice*; cambridge university press: 2009.
(103) Kfoury, J.; Benedek, Z.; Szilvási, T.; Oláh, J. H2 and N2 Binding Affinities Are Coupled in Synthetic Fe Nitrogenases Limiting N2 Fixation. *Organometallics.* **2022**, *41* (10), 1134−1146.
(104) Ma, W.; Zhang, J.-X.; Lin, Z.; Tilley, T. D.; Ye, Q. Synthesis, structure and DFT calculations of mononuclear cyclic (alkyl)(amino) carbene supported titanium (II) complexes. *Dalton Trans.* **2019**, *48* (40), 14962−14965.
(105) Horrer, G.; Krahfuß, M. J.; Lubitz, K.; Krummenacher, I.; Braunschweig, H.; Radius, U. N-Heterocyclic Carbene and Cyclic (Alkyl)(amino) carbene Complexes of Titanium (IV) and Titanium (III). *Eur. J. Inorg. Chem.* **2020**, *2020* (3), 281−291.

https://doi.org/10.1021/jacs.5c00099
J. Am. Chem. Soc. 2025, 147, 16948−16963